International Journal of Applied Earth Observation and Geoinformation 128 (2024) 103774

Contents lists available at ScienceDirect

International Journal of Applied Earth Observation and Geoinformation

journal homepage: www.elsevier.com/locate/jag

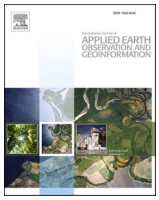

A semi-analytical approach for estimating inland water inherent optical properties and chlorophyll *a* using airborne hyperspectral imagery

Chao Niu [a,b], Kun Tan [a,b,*], Xue Wang [a,b], Peijun Du [c], Chen Pan [d]

[a] Key Laboratory of Geographic Information Science (Ministry of Education), East China Normal University, Shanghai 200241, China
[b] Key Laboratory of Spatial-Temporal Big Data Analysis and Application of Natural Resources in Megacities (Ministry of Natural Resources), East China Normal University, Shanghai 200241, China
[c] Jiangsu Provincial Key Laboratory of Geographic Information Science and Technology, Key Laboratory for Land Satellite Remote Sensing Applications of Ministry of Natural Resources, School of Geography and Ocean Science, Nanjing University, Nanjing 210023, Jiangsu, China
[d] Shanghai Municipal Institute of Surveying and Mapping, Shanghai 200063, China

ARTICLE INFO

Keywords:
Airborne hyperspectral
Inland water
Inherent optical properties
Chlorophyll *a*

ABSTRACT

The inversion of inherent optical properties (IOPs) and chlorophyll *a* (Chla) is one of the key objectives in water color remote sensing, and hyperspectral remote sensing with rich spectral information makes precise inversion possible. In this study, we developed a semi-analytical estimation method for inland water IOPs based on the quasi-analytical algorithm (QAA). Considering the complex optical characteristics of inland waters, empirical parameter regional optimization was conducted. Furthermore, a dual-band joint inversion strategy and Gaussian function fitting method were utilized to optimize the solution processes for the backscattering coefficient of particles (b_{bp}) and the absorption coefficient of phytoplankton pigments (a_{ph}), respectively. This approach overcomes the limitations of single-band b_{bp} inversion in inland waters. In addition, it directly decomposes the absorption coefficient to obtain a_{ph} using a Gaussian function, which can reduce the intermediate steps and errors caused by indirect inversion. For Chla, we constructed a binary inversion model using $a_{ph}(677)$ and remote sensing reflectance (R_{rs}), where the coefficient of determination (R^2) exceeded 0.8. We also constructed an airborne hyperspectral image correction process, including vicarious calibration, atmospheric correction, and bidirectional reflectance distribution function (BRDF) correction, obtaining high-precision R_{rs} images. The ground models were successfully applied to the airborne hyperspectral images, mapping the spatial distribution of IOPs and Chla concentration in the study area. The experiments demonstrated that the proposed semi-analytical method using airborne hyperspectral imagery exhibits a good performance in terms of modeling accuracy and mapping analysis, and successfully applied to long-term monitoring using satellite hyperspectral images, highlighting the significant potential of hyperspectral remote sensing for high-precision monitoring of regional water bodies.

1. Introduction

Remote sensing technology has the characteristics of large-scale and long-term monitoring and has been widely used in water environment monitoring. Due to the fact that the spectral characteristics of water bodies are mainly influenced by the water color, the use of optical remote sensing sensors for monitoring water bodies is also known as "water color remote sensing". One of the key objectives of water color remote sensing is the retrieval of inherent optical properties (IOPs) and chlorophyll *a* (Chla) (Werdell et al., 2018).

In addition to guiding the establishment of water color parameter retrieval models, IOPs also hold significant importance in revealing the role of water bodies in biogeochemical cycling processes. In the field of water color remote sensing, commonly used IOPs such as the absorption coefficient of phytoplankton pigments (a_{ph}) play a significant role in identifying the proportion of algae in water bodies, revealing the importance of water carbon cycling (Bricaud et al., 1995). The backscattering coefficient of water bodies holds significant potential in estimating the total suspended matter (TSM) content and particulate organic carbon (POC) (Allison et al., 2010), and also plays an important role in investigations of the optical properties of turbid inland waters and understanding the inherent mechanisms of transportation and

* Corresponding author.
E-mail address: tankuncu@gmail.com (K. Tan).

https://doi.org/10.1016/j.jag.2024.103774
Received 23 November 2023; Received in revised form 10 March 2024; Accepted 17 March 2024
Available online 22 March 2024

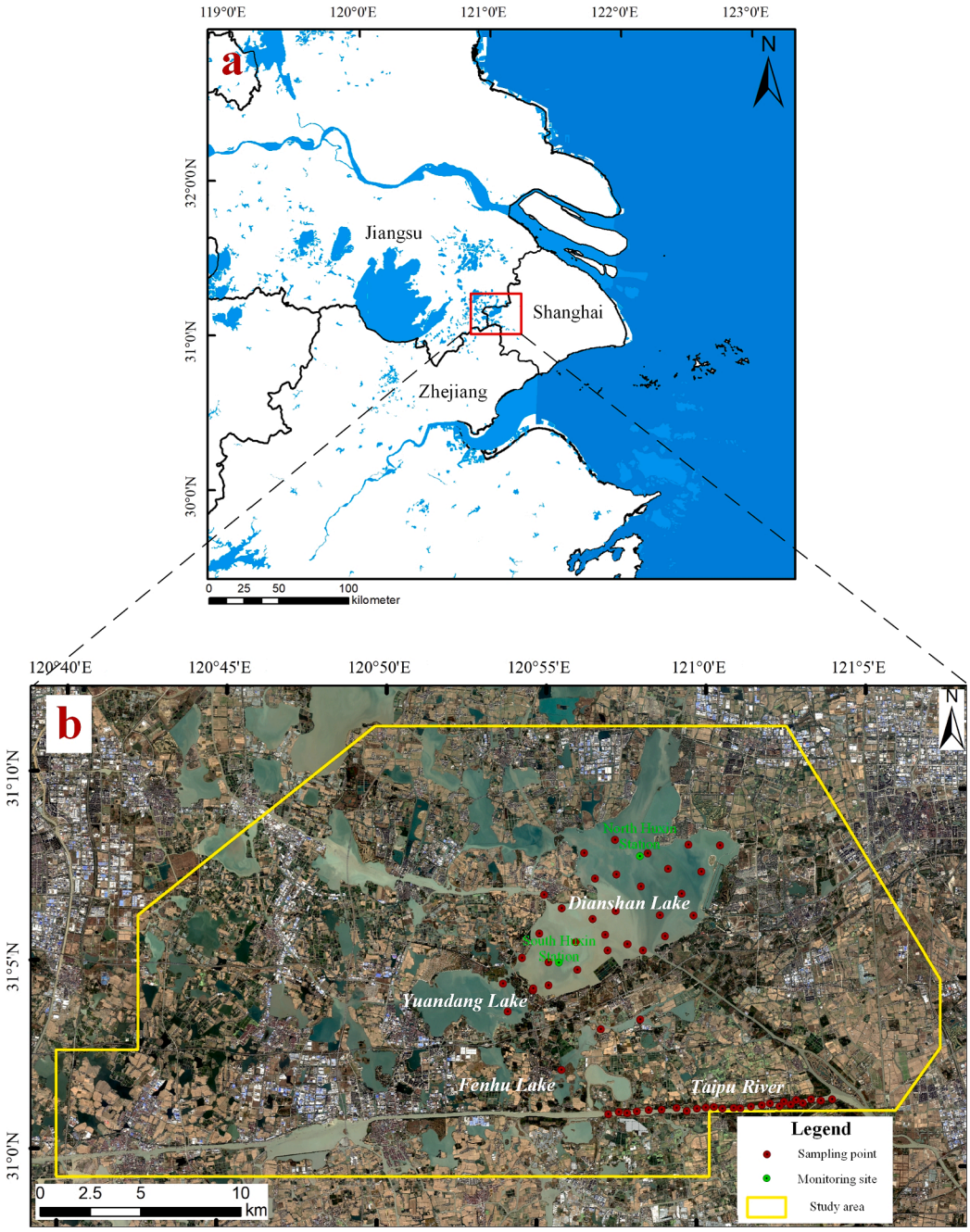

Fig. 1. The geographical location of the study area. (a) The location of the of the study area in China's administrative divisions. (b) Study area with sampling points and monitoring sites. The true color basemap is derived from Gaofen-6 satellite.

sedimentation of suspended particulate matter (Xu et al., 2021).

Using remote sensing techniques to retrieve IOPs primarily relies on constructing the relationships between the absorption and backscattering coefficients of various water constituents and apparent optical properties (AOPs), such as remote sensing reflectance (R_{rs}). The most commonly used methods include empirical (Lee et al., 1998) and semi-analytical (Gordon et al., 1988; Lee et al., 2002) methods. In addition, there are optimization algorithms (Zhan et al., 2003) and matrix inversion methods (Hoge and Lyon, 1996), etc. The optical characteristics of the oceanic Case-I waters are predominantly dominated by Chla and phytoplankton, for which both empirical and semi-analytical methods have been extensively employed. Coastal and inland waters, categorized as Case-II waters, exhibit complex optical properties influenced by multiple water components. Therefore, algorithms developed for Case-I waters cannot be directly applied to Case-II waters. Instead, parameter adjustments are necessary by considering the dominant regional optical characteristics (Ogashawara et al., 2016; Zhu and Yu, 2012). However, due to the regional variation of the optical characteristics of Case-II waters, there is an unavoidable contradiction between the universality and accuracy of the models.

Chla is a crucial water color parameter that can intuitively reflect the ecological environment of water bodies and plays an important indicative role in water environment monitoring. The optical properties of Case-I waters are relatively simple. By establishing a regression model based on the red and blue band ratio, good inversion results can be obtained, which is an approach that has been operationally utilized within water color remote sensing (Gordon and Morel, 1983). For coastal and inland Case-II waters, the spectral characteristics of Chla are

affected by other optically active substances, rendering Chla inversion models designed for Case-I waters inapplicable. Inversion algorithms based on three-band reflectance difference, four-band semi-analytical models, semi-analytical methods, and water optical property classification methods have been utilized for Chla estimation in inland and coastal waters (Neil et al., 2019). In order to improve the generalization of the model, researchers have established segmented inversion models for different water optical characteristics or Chla concentration ranges, to improve the inversion accuracy for Chla (He et al., 2020; Liu et al., 2020).

Currently, research on inland water color monitoring often utilizes multispectral images obtained from land-resource satellites. Although it can provide rich image information for monitoring inland water bodies, limited by the spectral resolution, multispectral sensors cannot accurately identify the sensitive features of water bodies under different optical characteristics. The airborne hyperspectral imagery has the characteristics of both a high-spatial resolution and a high-spectral resolution, giving them incomparable advantages over the traditional methods in the water quality monitoring of medium- and small-scale inland water bodies (Kim et al., 2022; Niu et al., 2021a). For inland water bodies, it is not only necessary to consider the impact of water optical characteristics, but it is also necessary to consider the differences in aerosol types. The multispectral bands of hyperspectral images also pose higher requirements for atmospheric correction. In the case of the widespread limitations in the water-atmospheric correction algorithms, land-atmospheric correction methods based on radiative transfer models are also used for water bodies, due to their ability to accurately simulate regional atmospheric conditions and the high spectral resolution (Xu et al., 2020). In addition, due to the bidirectional reflectance distribution function (BRDF) effects of water bodies and the different imaging conditions, the radiation intensity received by the different strips can be inconsistent, which affects the overall consistency of the imagery. Through BRDF correction, it is possible to significantly reduce the radiation differences between overlapping areas of the imagery and improve the reliability of receiving water radiation signals (Tan et al., 2020).

Most of the current water color remote sensing inversion models rely on ground-measured hyperspectral data to select sensitive bands and perform regression modeling. In the subsequent image inversion and mapping, due to the spectral resolution and band setting of the sensors, it is difficult for the optimal model on the ground to be directly transferred and applied to the imagery. The characteristic of multiple spectral bands in hyperspectral images can effectively compensate for this drawback. However, due to the different spectral resolutions and the different atmospheric disturbances suffered by sensor platforms, how to establish the spectral transfer process from “ground spectrum” to “airborne spectrum” and achieve the promotion of ground models to multi-source images is a major challenge in the application of hyperspectral water color imaging.

In summary, this study was aimed at the demand for precise monitoring of inland lakes and small rivers, where a semi-analytical inversion algorithm was constructed with the help of ground-measured hyperspectral data. At the same time, in order to ensure the transferability of the model, this study addressed hyperspectral image calibration, the elimination of atmospheric effects and the radiation differences caused by multiple imaging conditions, the acquisition of high-precision water-leaving reflectance data, the application of the ground model to airborne hyperspectral images, and the accurate inversion and mapping analysis of IOPs and Chla.

2. Materials

2.1. Study area

The study area for this experiment was located in the Yangtze River Delta Integration Development Demonstration Zone, situated at the junction of the city of Shanghai, Jiangsu province, and Zhejiang province. This area is located in the center of the most densely populated and economically developed urban agglomeration in China.

The flight area covered approximately 800 km^2, and the center of the area was located at 31.02°N, 120.89°E. The water bodies considered in this study are part of the Taihu Lake basin and include Taipu River, Dianshan Lake, Yuandang Lake, and Fenhu Lake. Dianshan Lake is the largest freshwater lake in Shanghai, covering a total area of about 62 km^2. Taipu River is the largest artificial river in the Taihu Lake basin, and also serves as a significant source of drinking water. The geographical location of the study area is shown in Fig. 1.

2.2. Data acquisition

2.2.1. Airborne hyperspectral image acquisition

The imaging spectrometer was the Airborne Multi-Modality Imaging Spectrometer (AMMIS) visible and near-infrared (VNIR) module developed by the Shanghai Institute of Technical Physics at the Chinese Academy of Sciences (Jia et al., 2021). The VNIR module features 256 bands covering a range of 400–1000 nm, with a IFOV of 0.25 mrad. The airborne hyperspectral image data were obtained with the imaging spectrometer mounted on a fixed-wing aircraft. The spectrometer was placed on a Leica PAV80 gyro-stabilized platform, and the position and the orientation data were obtained using a POS AV610 system.

The airborne hyperspectral data were obtained on June 15 and 16, 2022, with a flight direction of east–west, a speed of 200–240 km/hour, and a flight altitude of 3000 m. The time span from 08:30 to 10:30 with a lower solar angle, which will largely avoid sun glint. Finally, a total of 15 strips of images with a resolution of 0.75 m were obtained.

2.2.2. Field measurements

During the flight, water samples were quasi-synchronously collected at a depth of 50 cm, and the water spectra were measured using an ASD FieldSpec3 spectrometer. In addition, we also synchronously collected ground feature spectra for calibration. The radiance of a diffuse reflection standard board, the water surface, and the skylight were measured separately. The observation geometry refers to the NASA Ocean Optics Protocols for Satellite Ocean Color Sensor Validation document (Mueller et al., 2003). The remote sensing reflectance (R_{rs}) was calculated as follows:

$$R_{rs}(\lambda) = \frac{(L_w - rL_{sky})\rho_p}{\pi L_p}, \quad (1)$$

where L_w, L_{sky}, and L_p are the radiance of the water, sky, and the diffuse reflection standard board, respectively; ρ_p is the reflectance of the standard board; and r represents the reflectance of the skylight from the air–water interface (Mobley, 1999). 61 sets of sampling data were utilized for the modeling.

2.2.3. Laboratory tests

After completing the water sample collection, the water samples were filtered using 47-mm Whatman GF/F glass-fiber filters, and Chla was extracted using the 90 % hot ethanol extraction method. Chla concentration was then calculated by measuring the absorbance at 665 and 750 nm using an ultraviolet–visible spectrophotometer (Shimadzu UV-2700i). The absorption coefficients of phytoplankton pigments (a_{ph}) and detritus (a_d) were determined using the quantitative filter technique (Mitchell, 1990). The measurement of CDOM required water to be re-filtered through a 0.22 μm Millipore membrane filter, and the absorption coefficients for CDOM (a_g) were calculated using the spectrophotometer. The concentrations of Total Suspended Matter (TSM), Inorganic Suspended Matter (ISM) and Organic Suspended Matter (OSM) were determined using the gravimetric method (Wen et al., 2022).

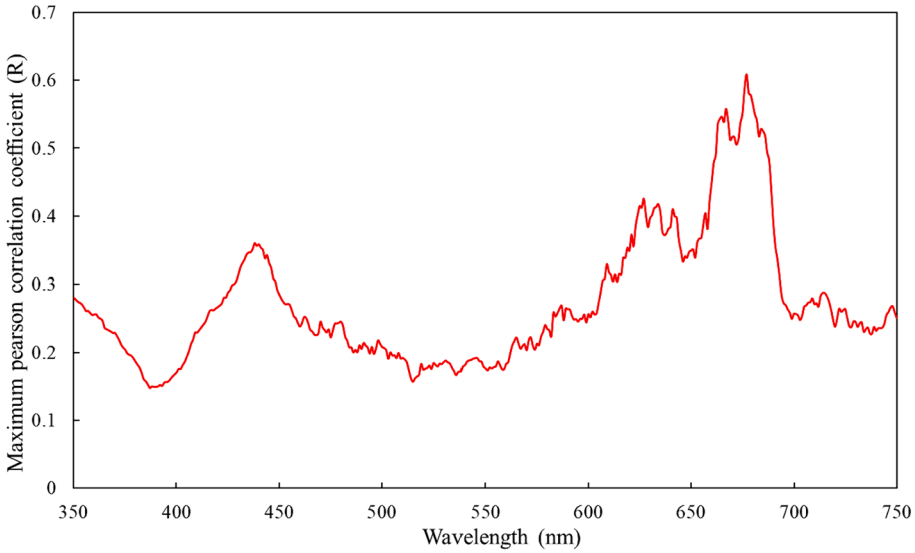

Fig. 2. Distribution of the maximum correlation between $a(\lambda_0)$ and R_{rs}.

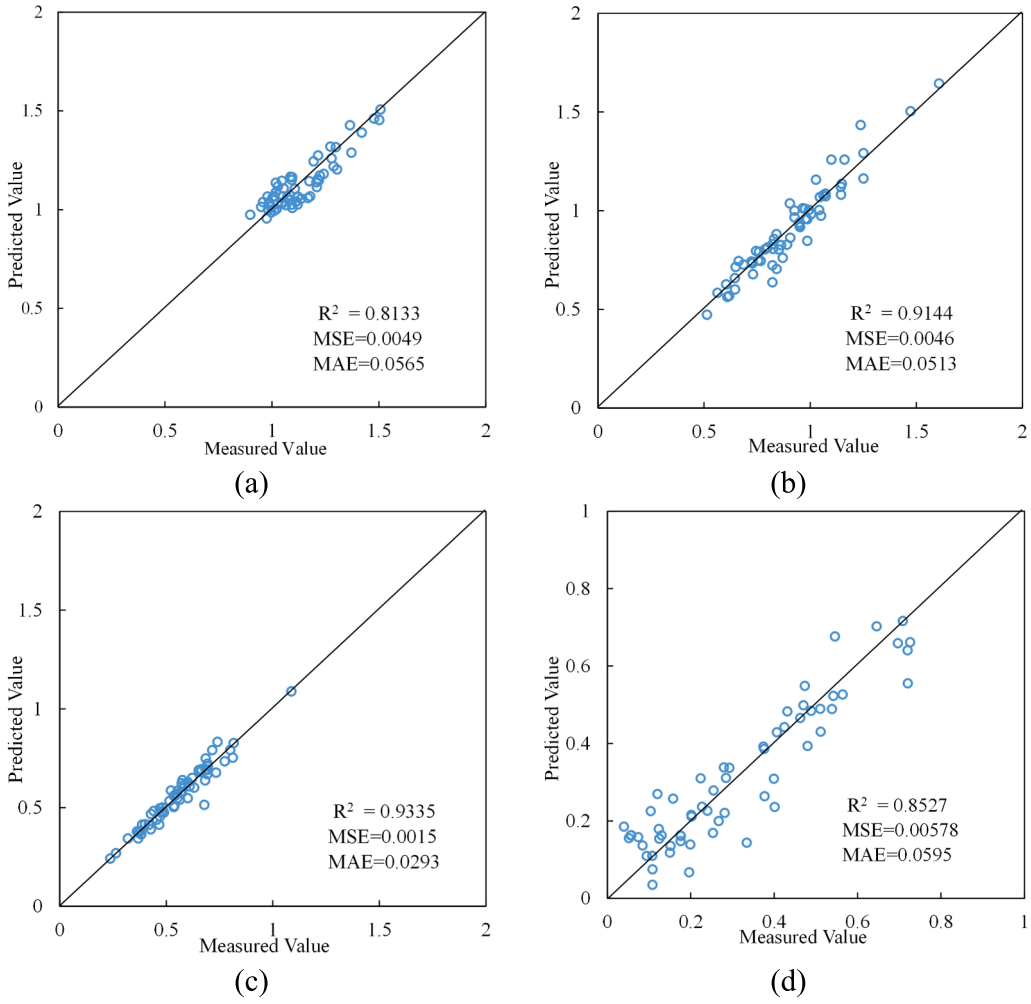

Fig. 3. Scatter plots of the predicted and measured values. (a) $a(\lambda_0)$. (b) $b_{bp}(550)$. (c) $b_{bp}(\lambda_0)$. (d) $a_{ph}(677)$.

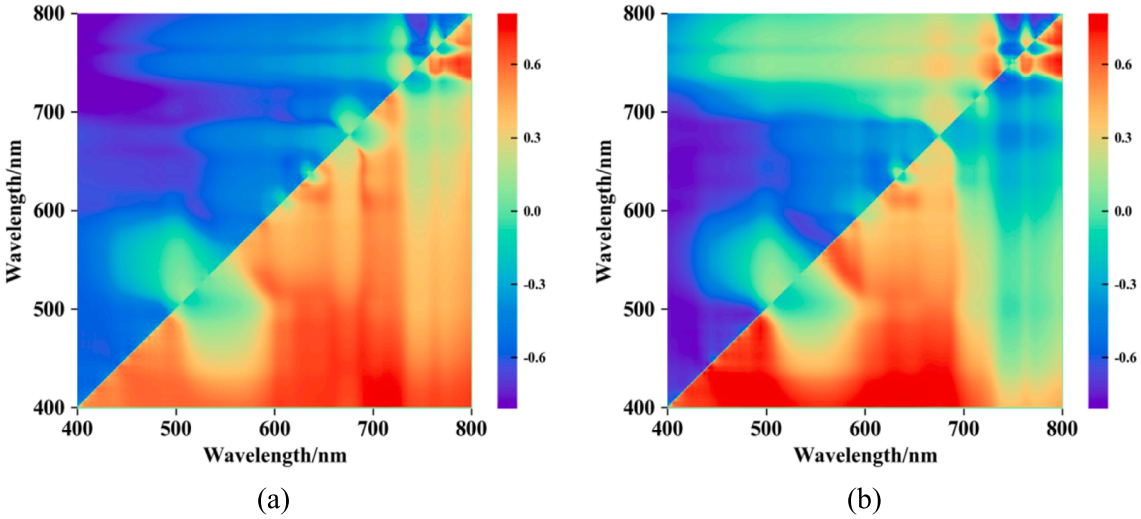

Fig. 4. The correlation between the band ratio the in r_{rs} and η. (a) η550. (b) η677.

Table 1
The Gaussian function parameterization settings for the main pigments. Chl: chlorophyll; PPC: photoprotective carotenoids; PSC: photosynthetic carotenoids; PE: phycoerythrin.

Pigments (nm)	Chla&c	Chla	Chl b&c	Chl b	PPC	PSC	PE	Chl c	Chla	Chl c	Chl b	Chla
Initial peak	409	437	457	467	491	527	552	585	620	639	658	676
Initial standard deviation	15	15	15	15	15	15	15	15	15	15	15	15
Initial height of peak	1	1	1	1	1	1	1	1	1	1	1	1
Peak range	-5–5	-5–5	-5–5	-5–5	-5–5	-5–5	-5–5	-5–5	-5–5	-5–5	-5–5	-5–5
Standard deviation range	5–50	5–50	5–50	5–50	5–50	5–50	5–50	5–50	5–50	5–50	5–50	5–50
Height range	0–2	0–2	0–2	0–2	0–2	0–2	0–2	0–2	0–2	0–2	0–2	0–2
Final peak	407.3	438.2	453.5	468.8	492.3	525.8	553.0	584.9	618.3	648.9	664.7	679.3
Final standard deviation	30.59	18.41	14.98	14.79	24.45	19.63	20.70	23.09	21.44	19.63	42.29	18.07
Final height of peak	1.61	0.88	0.40	0.53	0.83	0.22	0.43	0.49	0.40	0.22	0.70	0.46

3. Method

3.1. IOP estimation using the proposed QAA_gauss model

The proposed semi-analytical algorithm is based on the QAA algorithm, and is combined with empirical formulas for regional parameter optimization and a Gaussian function fitting method to improve its applicability in the target water area. The proposed model is named the QAA_gauss model.

The QAA_gauss model is divided into two parts. The first part derives the total absorption coefficient a(λ) and the backward scattering coefficient $b_b(\lambda)$ using the improved algorithm based on regional parameter optimization. a(λ) consists of four parts: the pure water absorption coefficient (a_w), a_{ph}, a_d, and a_g. After solving a(λ), the absorption coefficients corresponding to each water component can be decomposed. The second step is to decompose a(λ) to obtain $a_{ph}(\lambda)$. The processing steps are briefly described as follows.

3.1.1. Calculate a and b_b

Step 1: convert the R_{rs} to the subsurface remote sensing reflectance (r_{rs}), following Lee et al. (2002):

$$r_{rs}(\lambda) = \frac{R_{rs}(\lambda)}{0.52 + 1.7 \times R_{rs}(\lambda)}. \tag{2}$$

Step 2: according to the radiative transfer process, r_{rs} can be described as a function of $b_b/(a + b_b)$ (Gordon et al., 1988). Make $u(\lambda) = b_b/(a + b_b)$, according to the empirical constant obtained by Lee et al. (2002), where $u(\lambda)$ can be expressed in the following form:

$$u(\lambda) = \frac{-g_0 + \sqrt{g_0^2 + 4g_1 \cdot r_{rs}(\lambda)}}{2g_1}, \tag{3}$$

where $g_0 = 0.089$, $g_1 = 0.1245$.

Step 3: determine the reference wavelength λ_0 and obtain the corresponding $a(\lambda_0)$. In the QAA algorithm, the reference wavelength λ_0 requires us to consider the simulation effect of the backscattering coefficient. It is necessary to ensure that pure water dominates at the reference wavelength and that $a(\lambda_0)$ can be accurately estimated (Lee et al., 2002). Based on this, a Pearson correlation analysis is utilized to find the $a(\lambda_0)$ with the highest absolute correlation with R_{rs}, where λ_0 is the reference wavelength. The correlation distribution is shown in Fig. 2. The highest absolute correlation is at 677 nm, which was selected as the reference wavelength.

Referencing the three-band calculation form provided by the latest version of QAA_V6 (Lee et al., 2014) for turbid water bodies, the empirical formula is obtained through band optimization:

$$a(\lambda_0) = a_w(\lambda_0) - 24.447 \times \frac{R_{rs}(510)}{R_{rs}(496) + R_{rs}(527)} + 13.131, \tag{4}$$

where $a_w(\lambda_0)$ is the absorption coefficient of pure water at wavelength λ_0. The scatter plot of the measured and predicted $a(\lambda_0)$ is shown in Fig. 3 (a).

Table 2
Steps of the QAA_gauss method to derive IOPs using R_{rs}.

Step	Property	Formula	Approach
1	r_{rs}	$r_{rs}(\lambda) = \frac{R_{rs}(\lambda)}{0.52 + 1.7 \times R_{rs}(\lambda)}$.	Semi-analytical
2	$u(\lambda)$	$u(\lambda) = \frac{-g_0 + \sqrt{g_0^2 + 4g_1 \cdot r_{rs}(\lambda)}}{2g_1}$, $g_0 = 0.089, g_1 = 0.1245$	Semi-analytical
3	$a(\lambda_0)$	$a(\lambda_0) = a_w(\lambda_0) - 24.447 \times \frac{R_{rs}(510)}{R_{rs}(496) + R_{rs}(527)} + 13.131, \lambda_0 = 677$	Empirical
4	$b_{bp}(550)$	$b_{bp}(550) = 25.739 \times R_{rs}(527) - 0.0418$	Empirical
5	$b_{bp}(\lambda_0)$	$b_{bp}(\lambda_0) = \frac{u(\lambda_0)a(\lambda_0)}{1 - u(\lambda_0)} - b_{bw}(\lambda_0)$	Analytical
6	$\eta 550$	$\eta 550 = -1.133 \times \left[\frac{r_{rs}(425)}{r_{rs}(718)}\right]^2 + 5.053 \times \frac{r_{rs}(425)}{r_{rs}(718)} - 3.135$	Empirical
7	$\eta 677$	$\eta 677 = -1.575 \times \left[\frac{r_{rs}(425)}{r_{rs}(687)}\right]^2 + 5.369 \times \frac{r_{rs}(425)}{r_{rs}(687)} - 1.780$	Empirical
8	$b_{bp}(\lambda)$	$b_{bp}(\lambda) = S1 \cdot b_{bp}(550)\left(\frac{550}{\lambda}\right)^{\eta 550} + S2 \cdot b_{bp}(677)\left(\frac{677}{\lambda}\right)^{\eta 677}$	Optimization
9	$a(\lambda)$	$a(\lambda) = \frac{[1 - u(\lambda_0)] \times [b_{bw}(\lambda) + b_{bp}(\lambda_0)]}{u(\lambda_0)}$	Analytical
10	$a_{ph}(677)$	$a_{ph}(677) = -0.901 \times a(550) + 1.290 \times a(677) - 0.207$	Empirical
11	$a_{ph}(\lambda)$	$a_{ph}(\lambda) = a_{ph}(677) \times \sum_{12}^{i=1} k_i(\lambda) e^{-\frac{(\lambda - \mu_i)^2}{2\sigma_i^2}}$	Semi-analytical

Table 3
Model parameters and regression formulas.

Number of variables	Input parameters	Regression models
a univariate inversion model: Chla = $f(x)$	$a_{ph}(677)$ $R_{rs}(677)$ $R_{rs}(a)/R_{rs}(b)$ $[R_{rs}(a) - R_{rs}(b)]/[R_{rs}(a) + R_{rs}(b)]$ $(R_{rs}(a)^{-1} - R_{rs}(b)^{-1}) \times R_{rs}(c)$ $R_{rs}(a)/[R_{rs}(a) - R_{rs}(b)]$	linear: (ax + b) quadratic polynomial: (ax^2 + bx + c) exponential function: (ax^b)
a binary inversion model: Chla = $f(x, y)$	($a_{ph}(677)$, $R_{rs}(a)/R_{rs}(b)$) ($a_{ph}(677)$, $[R_{rs}(a) - R_{rs}(b)]/[R_{rs}(a) + R_{rs}(b)]$) ($a_{ph}(677)$, $(R_{rs}(a)^{-1} - R_{rs}(b)^{-1}) \times R_{rs}(c)$) ($a_{ph}(677)$, $R_{rs}(a)/[R_{rs}(a) - R_{rs}(b)]$)	bivariate linear: (ax + by + c) bivariate quadratic polynomial: ($ax^2 + bx + cy^2 + dy + e$) bivariate exponential function: ($ax^b + cy^d$)

Step 4 and Step 5: calculate the backscattering coefficient of particles at the reference wavelength $b_{bp}(\lambda_0)$.

The backscattering coefficient is usually expressed as the sum of the backscattering coefficient of pure water b_{bw} and the backscattering coefficient of particles b_{bp}. b_{bp} is generally considered to have a power function relationship with $b_{bp}(\lambda_0)$ (Gordon and Morel, 1983). Therefore, $b_{bp}(\lambda_0)$ and η are the key to calculating b_b.

$$b_b(\lambda) = b_{bw}(\lambda) + b_{bp}(\lambda_0)\left(\frac{\lambda_0}{\lambda}\right)^{\eta}. \quad (5)$$

Due to the technical difficulties in measuring the backscatter coefficient in turbid shallow water, b_{bp} was not measured in this experiment. Based on the optical closure theory, the simulation of b_{bp} using the measured absorption coefficient and reflectance has been successfully applied to the eutrophic water in Taihu Lake basin (Pan et al., 2015; Tzortziou et al., 2006). This study utilized the calculated $u(\lambda)$ by Eq. (2) and the measured a(λ) to simulated particle backscatter coefficient as the reference particle backscatter coefficient, and the formula is as follows.

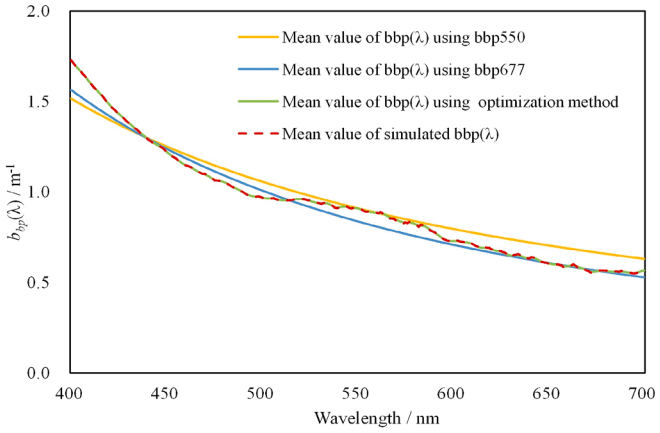

Fig. 5. The mean values of $b_{bp}(\lambda)$.

$$b_{bp\_sim}(\lambda) = \frac{u(\lambda)a_{measured}(\lambda)}{1 - u(\lambda)} - b_{bw}(\lambda), \quad (6)$$

where the range of λ is from 400 to 700 nm. When λ is greater than 700 nm, $b_{bp\_sim}(\lambda) = b_{bp\_sim}(700)$.

Previous studies have shown that for the near-infrared region where particles have lower light absorption, the power function fits well (Doxaran et al., 2009; Shi et al., 2014). However, using a single wavelength for power function fitting has a significant deviation for the visible spectrum where particles absorb more light (Doxaran et al., 2007). In addition, the absorption characteristics of different particles also have an impact on the scattering coefficient (Snyder et al., 2008). Therefore, we also added 550 nm as the second reference wavelength, which is an intermediate wavelength between visible and near-infrared, to better characterize the absorption characteristics of different particles. The corresponding backscattering coefficient of particles was calculated separately.

$b_{bp}(\lambda_0)$ was obtained by the semi-analytical formula in the QAA algorithm, and $b_{bp}(550)$ was fitted by a linear empirical formula. The scatter plots of the measured and predicted $b_{bp}(550)$ and $b_{bp}(\lambda_0)$ are shown in Fig. 3(b) and Fig. 3(c), respectively.

$$b_{bp}(550) = 25.739 \times R_{rs}(527) - 0.0418 \quad (7)$$

$$b_{bp}(\lambda_0) = \frac{u(\lambda_0)a(\lambda_0)}{1 - u(\lambda_0)} - b_{bw}(\lambda_0) \quad (8)$$

Step 6 and Step 7: calculate the power law exponent value $\eta 550$ and $\eta 677$ by searching for the optimal band ratio in r_{rs} and establishing a quadratic function empirical equation. The correlation distribution maps between the band ratio in r_{rs} and $\eta 550$, $\eta 677$ are shown in Fig. 4. For $\eta 550$, the band ratio corresponding to the maximum correlation is ($r_{rs}425$)/($r_{rs}718$). For $\eta 677$ is ($r_{rs}425$)/($r_{rs}687$). The empirical formulas are as follows.

$$\eta 550 = -1.133 \times \left[\frac{r_{rs}(425)}{r_{rs}(718)}\right]^2 + 5.053 \times \frac{r_{rs}(425)}{r_{rs}(718)} - 3.135 \quad (9)$$

$$\eta 677 = -1.575 \times \left[\frac{r_{rs}(425)}{r_{rs}(687)}\right]^2 + 5.369 \times \frac{r_{rs}(425)}{r_{rs}(687)} - 1.780 \quad (10)$$

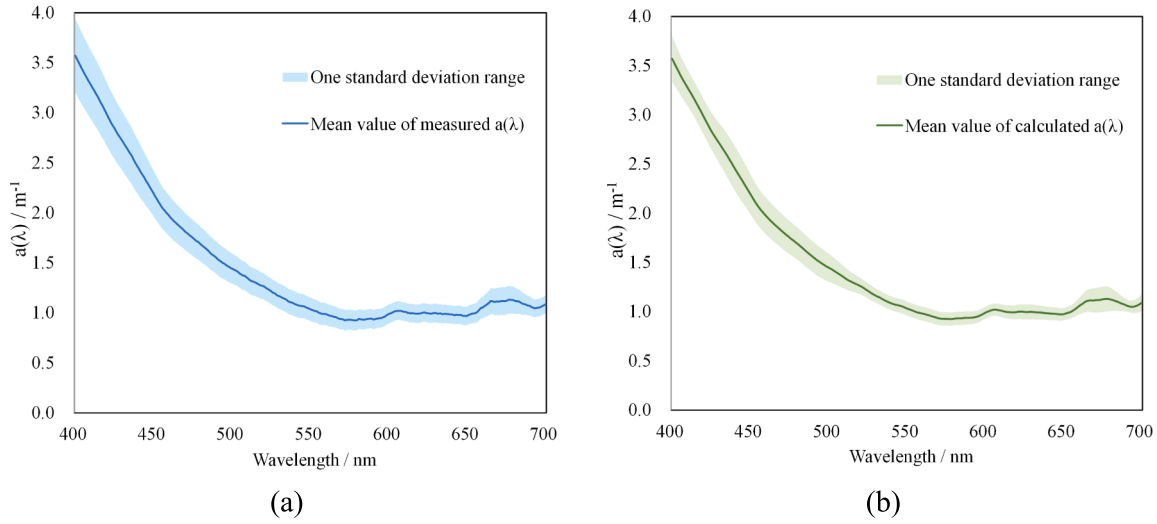

Fig. 6. Comparison of the mean $a(\lambda)$ value. (a) The measured $a(\lambda)$. (b) The calculated $a(\lambda)$. The shaded area is one standard deviation around the mean value.

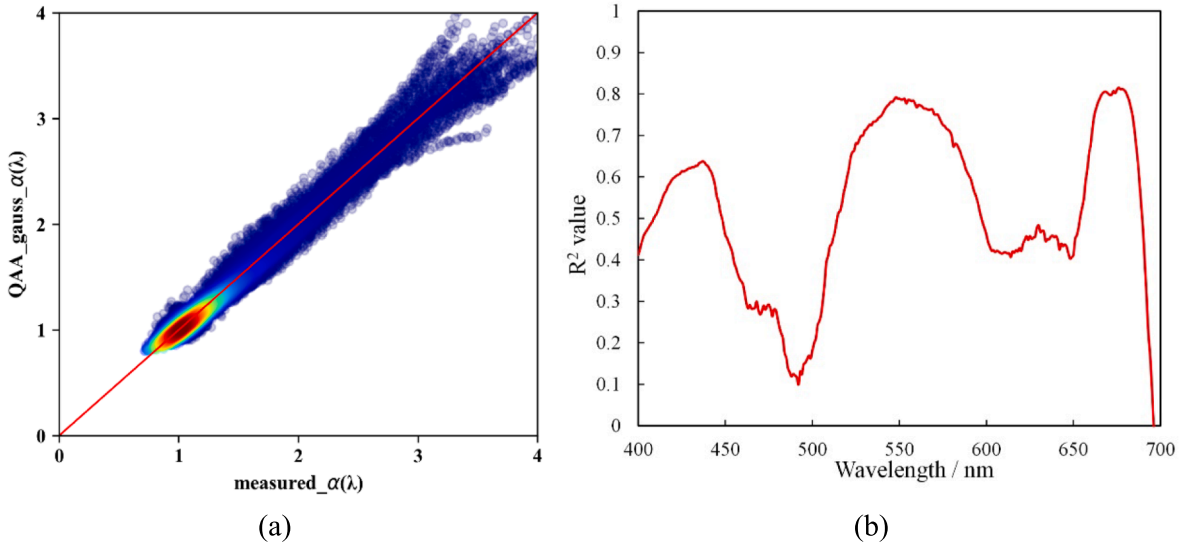

Fig. 7. Distribution and accuracy of the calculated $a(\lambda)$ obtained using the field-measured spectra. (a) Density scatter plot of the measured and calculated $a(\lambda)$. (b) R^2 distribution of each band.

Step 8: combined with the dual-band joint inversion strategy in Step 4 and Step 5, the overall solution equation for the backscattering coefficient is as follows:

$$b_{bp}(\lambda) = S1 \cdot b_{bp}(550)\left(\frac{550}{\lambda}\right)^{\eta 550} + S2 \cdot b_{bp}(677)\left(\frac{677}{\lambda}\right)^{\eta 677}, \quad (11)$$

where $S1$ and $S2$ are the model parameters obtained using the least-squares method.

Step 9: after calculating all the parameters, $a(\lambda)$ can be calculated through $u(\lambda)$ in Step 2.

$$a(\lambda) = \frac{[1 - u(\lambda_0)] \times [b_{bw}(\lambda) + b_{bp}(\lambda_0)]}{u(\lambda_0)}. \quad (12)$$

3.1.2. A_{ph} Gaussian function simulation

The QAA_V6 algorithm empirically estimates the ratio of a_{ph} and a_{dg} at 412 nm and 443 nm, and extends to the whole wavelength based on the exponential decay relationship between a_{dg} and the wavelength. However, due to the significant differences in particulate matter content in inland water bodies, estimating a_{dg} using spectral attenuation coefficients can lead to significant errors.

There are multiple absorption peaks in a_{ph}, corresponding to the absorption of pigment substances such as chlorophyll, carotene, and phycoerythrin. Since the Gaussian shape can represent the absorption spectrum of a single photosynthetic component well, using a Gaussian function with the spectral absorption characteristics is an important way to simulate a_{ph} (Hoepffner and Sathyendranath, 1991). Referring to previous studies on the characteristic wavelengths of absorption peaks corresponding to pigment substances (Chase et al., 2013; Hoepffner and Sathyendranath, 1993), a Gaussian simulation function with 12 main pigments was constructed by setting the initial absorption peak wavelength (μ), initial standard deviation (σ), and initial height of peak (k).

$$a'_{ph}(\lambda) = \sum_{12}^{i=1} k_i(\lambda) e^{-\frac{(\lambda-\mu_i)^2}{2\sigma_i^2}}, \quad (13)$$

where a'_{ph} is the simulated a_{ph}, and i is the pigment substances. Here, we introduced $a_{ph}(677)$ as a scaling factor to globally adjust the value of

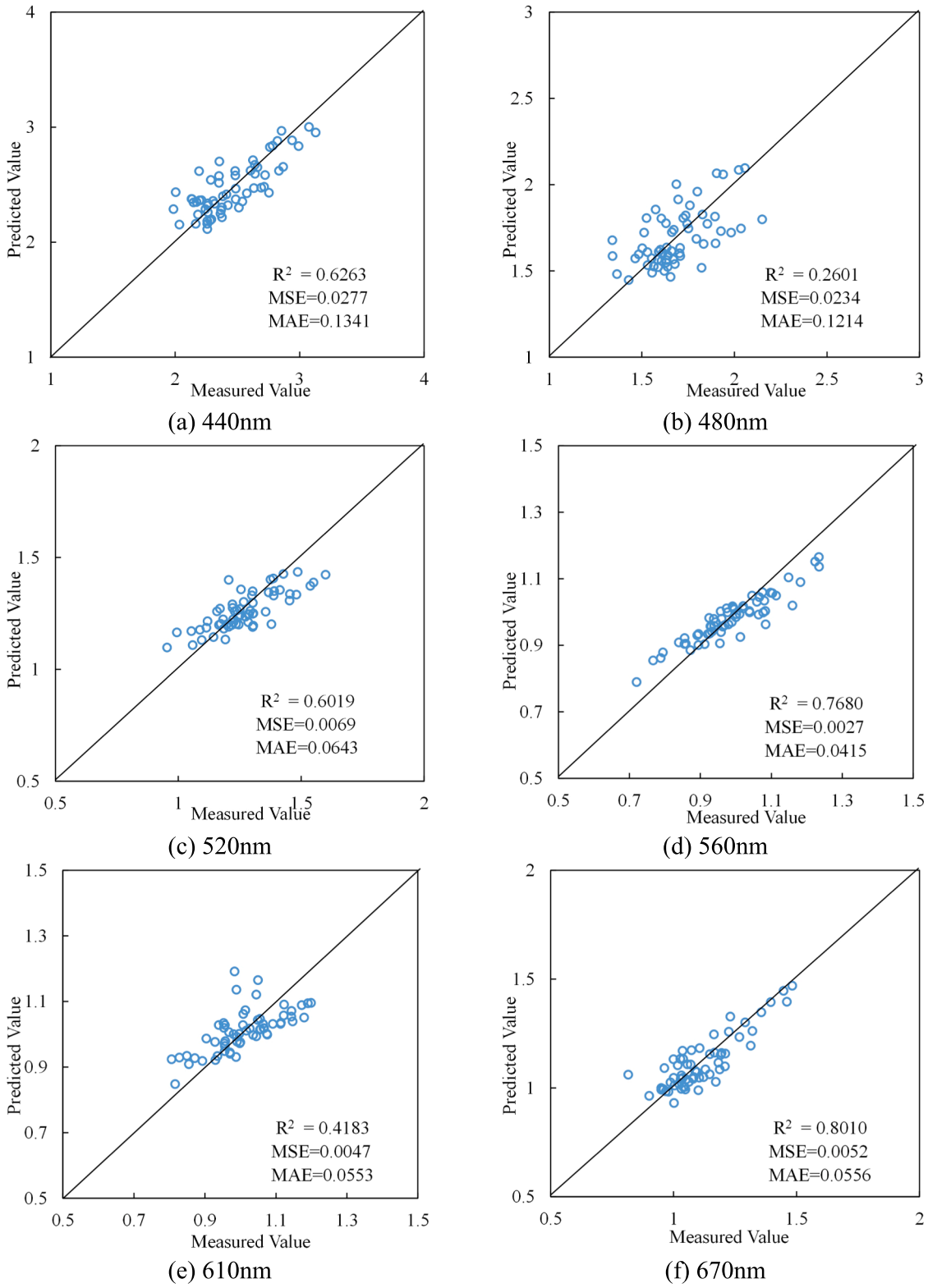

Fig. 8. Scatter plot distribution of the calculated and measured $a(\lambda)$.

$a_{ph}(\lambda)$. Based on the measured a_{ph} data, a constrained least-squares model was established by limiting the parameter range of the Gaussian function. The constraint formula is shown in Eq. (14), and the optimal Gaussian parameters were solved using the least-squares method.

$$\operatorname{argmin}\left(a_{ph}(\lambda,n)-a_{ph(\lambda=677,n)}\times\sum_{12}^{i=1}k_i(\lambda)e^{-\frac{(\lambda-\mu_i)^2}{2\sigma_i^2}}\right),\quad s.t.\quad 0\leqslant k\leqslant 2,\ -5\leqslant\mu\leqslant 5,\ 5\leqslant\sigma\leqslant 50 \tag{14}$$

where n is the number of samples, $a_{ph}(\lambda,n)$ is the measured a_{ph} data of

Table 4
Inversion accuracy for $a(\lambda)$.

Wavelength	R^2	MSE	MAE
440	0.6263	0.0277	0.1341
480	0.2601	0.0234	0.1214
520	0.6019	0.0069	0.0643
560	0.7680	0.0027	0.0415
610	0.4183	0.0047	0.0553
670	0.8010	0.0052	0.0556
Overall	0.9627	0.0117	0.0886

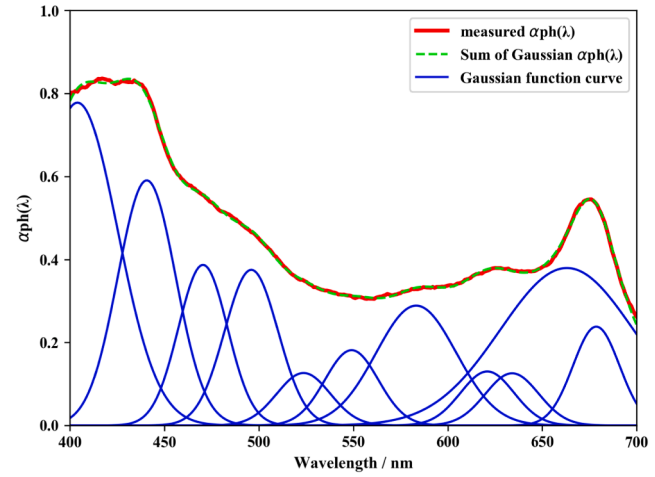

(a)

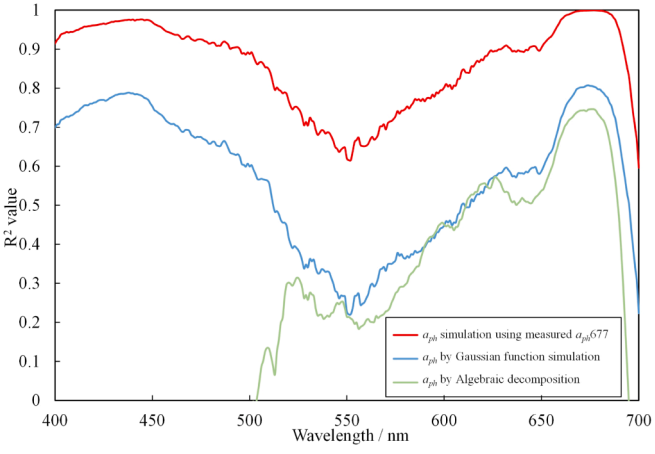

(b)

Fig. 9. Gaussian function simulation and accuracy of the calculated $a_{ph}(\lambda)$. (a) The Gaussian function curve and simulated $a_{ph}(\lambda)$. (b) R^2 distribution for $a_{ph}(\lambda)$.

sample n, and $a_{ph(\lambda=677,n)}$ is the measured $a_{ph}(677)$ of sample n. The Gaussian function parameterization settings for the main pigments and parameter range limitations are listed in Table 1.

3.1.3. $a(\lambda)$ decomposition based on a_{ph} simulation

In order to establish the relationship between $a(\lambda)$ and $a_{ph}(\lambda)$, the linear relationship between $a(\lambda)$ and $a_{ph}(677)$ should be determined first. Because $a(677)$ is mainly dominated by a_w and a_{ph}, while $a(550)$ is dominated by particulate matter, the total absorption coefficients at 550 nm and 677 nm were utilized to construct a binary linear equation to obtain $a_{ph}(677)$. The scatter plot is shown in Fig. 3(d).

$$a_{ph}(677) = -0.901 \times a(550) + 1.290 \times a(677) - 0.207. \quad (15)$$

Substituting the optimization parameters calculated by Eq. (14), the Gaussian-simulated a_{ph} obtained from $a(\lambda)$ is calculated in Eq. (16). Finally, the inversion steps of the QAA_gauss method are shown in Table 2.

$$a_{ph}(\lambda) = a_{ph}(677) \times \sum_{12}^{i=1} k_i(\lambda) e^{-\frac{(\lambda-\mu_i)^2}{2\sigma_i^2}}. \quad (16)$$

3.2. Airborne hyperspectral image correction

When applying the established ground model to an airborne hyperspectral image, the accuracy of the atmospheric correction directly affects the model performance. Especially for inland water bodies, not only does the attenuation of the sensor's calibration coefficient need to be considered, but also the impact of atmospheric condition changes and the BRDF at the different imaging times. Based on this, we constructed an image correction process consisting of vicarious calibration, atmospheric correction, and BRDF correction, to achieve precise water-leaving radiation information acquisition. The hyperspectral image correction was implemented using the MODerate resolution atmospheric TRANsmission (MODTRAN) radiative transfer model (Berk et al., 1989) and Python programming language.

3.2.1. Vicarious calibration

In this study, we utilized a reflectance-based vicarious calibration method to calibrate the airborne hyperspectral imaging spectrometer. During the flight, the reflectance of the ground features, as well as meteorological parameters were synchronously measured. The radiance value of the sensor at the entrance pupil was calculated using the MODTRAN model, thereby solving the calibration coefficient. The calculation process refers to Niu et al., (2021b), where, after obtaining the measured surface reflectance ρ_s, the top of atmosphere radiance can be expressed as follows:

$$L = L_p + \frac{\rho_s}{1 - S\rho_s} F, \quad (17)$$

where L_p is the path radiance, S is the spherical albedo of the atmosphere, and F is the product of the total downward solar radiation and the atmospheric transmittance. These parameters can be solved using the MODTRAN model. ρ_s uses the measured water bodies, bare soil and grassland. After this, the relationship between the DN value and the entrance pupil radiance could be established, and the calibration coefficient could be obtained using the least-squares method.

3.2.2. Atmospheric correction

After vicarious calibration, the top of atmosphere radiance data can be calculated using the calibration coefficient. We utilized the MODTRAN radiative transfer model for atmospheric correction based on the meteorological parameters and observation geometry acquired from different stirp, and obtained surface reflectance data. The normalized difference water index (NDWI) was utilized for the water extraction. R_{rs} was finally calculated by dividing the surface reflectance of the water body by π. The calculation formula is as follows.

$$R_{rs} = \frac{L - L_p}{\pi[F + (L - L_p)S]}. \quad (18)$$

In subsequent model applications, due to the differences in spectral channel settings, the optimal ground-based model cannot be directly applied to images. Firstly, the Savitzky-Golay filter was utilized to eliminate spectral noise. In addition, considering the characteristics of the high correlation between adjacent bands of hyperspectral images, the spectral channels were resampled to be consistent with the ground-measured spectral channels.

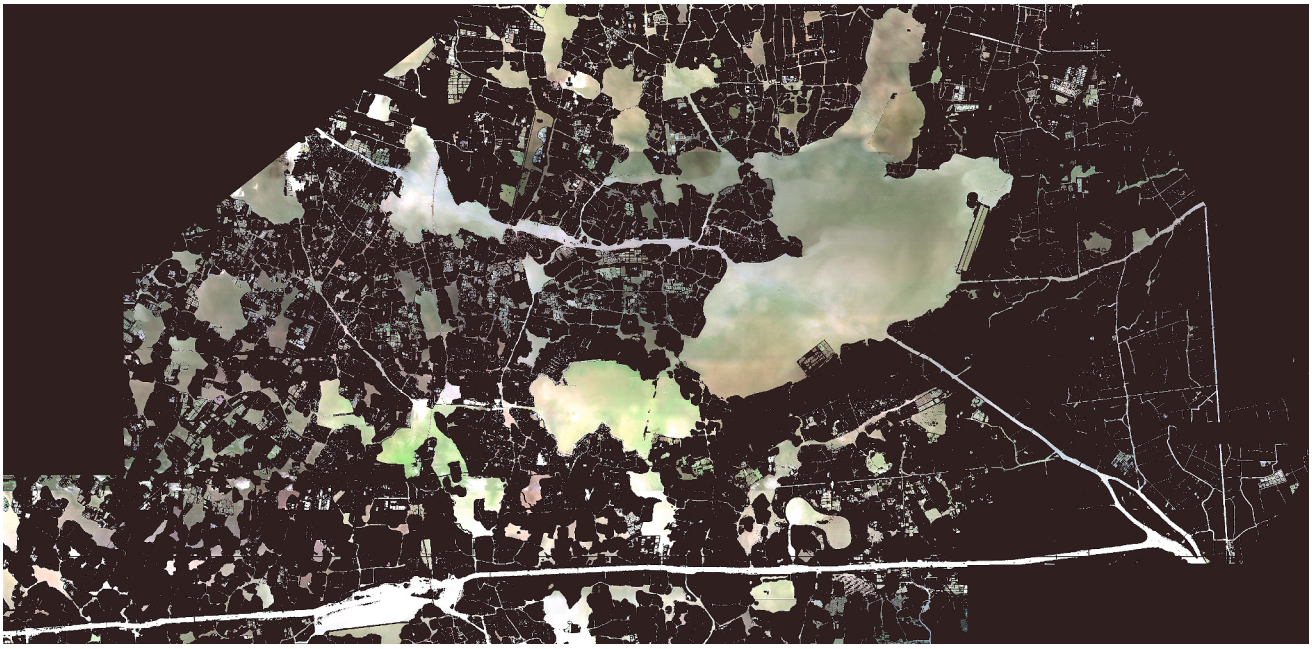

Fig. 10. The overall mosaicked image of the water bodies in the study area. RGB color composition with 639.02 nm, 550.87 nm and 460.64 nm.

Table 5
Comparison of the accuracy of $a_{ph}(\lambda)$.

Wavelength	Algebraic decomposition			Gaussian function simulation		
	R^2	MSE	MAE	R^2	MSE	MAE
440	−0.0832	0.1141	0.2980	0.7860	0.0225	0.1240
550	0.2144	0.0074	0.0707	0.2490	0.0071	0.0663
670	0.7428	0.0098	0.0810	0.8017	0.0076	0.0730
Overall	0.2282	0.0366	0.1335	0.8037	0.0090	0.0785

3.2.3. BRDF correction

Water bodies are affected by the BRDF effect, resulting in significant radiation differences under different sensor viewing angles and solar zenith angles, leading to the destruction of image consistency and a significant brightness gradient in the mosaicked image. To this end, we utilized a kernel-based BRDF correction model to eliminate the BRDF effect.

$$\rho(\theta_v, \theta_s, \Delta\varphi) = f_{iso} + f_{vol}K_{vol}(\theta_v, \theta_s, \Delta\varphi) + f_{\text{geo}}K_{\text{geo}}(\theta_v, \theta_s, \Delta\varphi), \quad (19)$$

where f is the model coefficient; K_{vol} and K_{geo} are the volumetric and geometric kernels, respectively; and Ross-Thick and Li-Sparse kernels are utilized to construct a calibration model (Wanner et al., 1995).

3.3. Chla inversion model

Due to the strong absorption characteristics of Chla in the red bands, $a_{ph}(677)$ are selected to invert Chla. However, the increase in the proportion of detritus particles (Cleveland, 1995) and the pigment packaging effect (Lohrenz et al., 2003; Stuart et al., 1998) will lead to a nonlinear relationship between a_{ph} and Chla. In this case, we additionally utilized the spectral characteristics of R_{rs}, established a binary inversion model, where the input parameters of the inversion model included x: $a_{ph}(677)$ (highly correlated with Chla) and y: R_{rs}. To reduce the errors caused by incomplete atmospheric correction, we conducted multiple

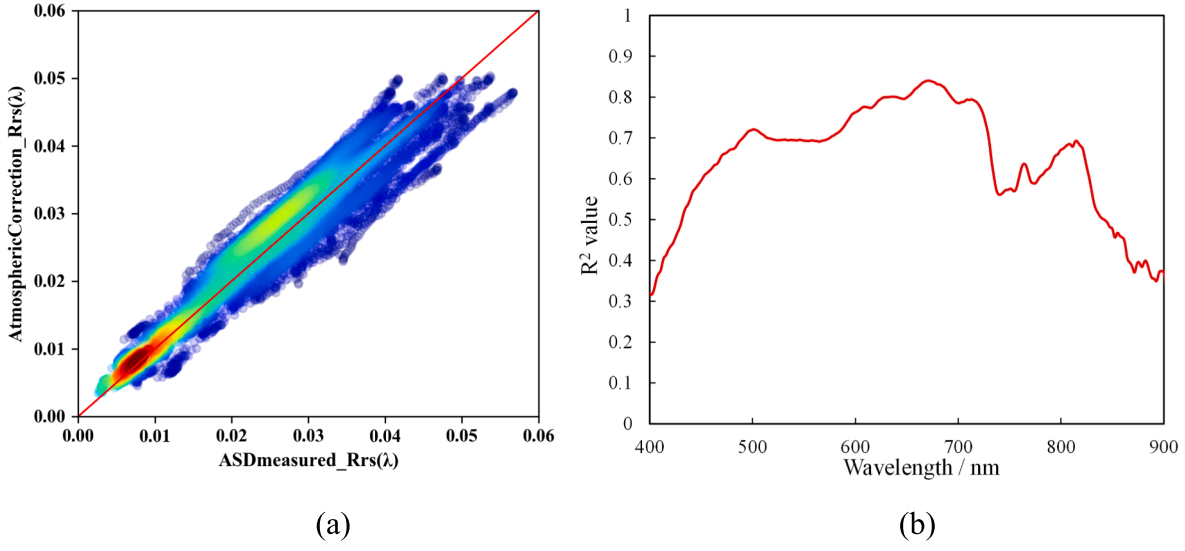

Fig. 11. Distribution and accuracy of the calculated $R_{rs}(\lambda)$. (a) Density scatter plot. (b) R^2 distribution for each band.

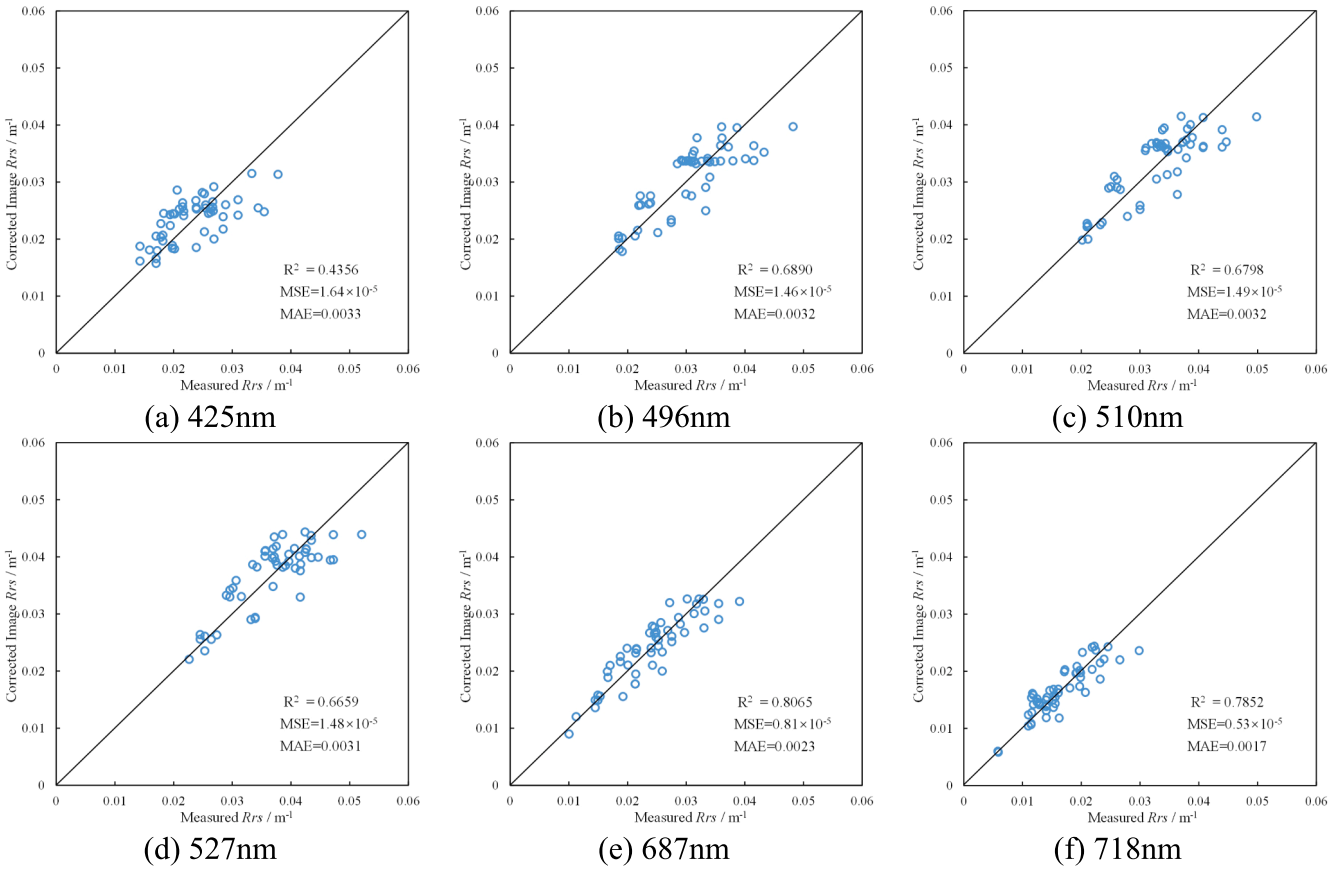

Fig. 12. Scatter plot distribution of the calculated and measured $R_{rs}(\lambda)$.

Table 6
Inversion accuracy for $R_{rs}(\lambda)$.

Wavelength	R^2	MSE	MAE
425	0.4356	0.0000164	0.0033
496	0.6890	0.0000146	0.0031
510	0.6798	0.0000149	0.0032
527	0.6659	0.0000148	0.0031
687	0.8065	0.0000081	0.0023
718	0.7852	0.0000053	0.0017
Overall	0.9498	0.0000096	0.0023

band ratio calculations on R_{rs} (Hu et al., 2012). The input R_{rs} included four types, i.e., the band ratio: $R_{rs}(a)/R_{rs}(b)$, the two-band difference ratio: $[R_{rs}(a) - R_{rs}(b)]/[R_{rs}(a) + R_{rs}(b)]$, the three-band algorithm: $(R_{rs}(a)^{-1} - R_{rs}(b)^{-1}) \times R_{rs}(c)$, and the advanced three-band algorithm: $R_{rs}(a)/[R_{rs}(b) - R_{rs}(c)]$ (Neil et al., 2019). In addition, we also used a univariate inversion model with R_{rs} or $a_{ph}(677)$ for comparison. The regression models were the commonly used regression model. The specific model parameters and regression formulas are listed in Table 3.

3.4. Model evaluation

The IOPs and Chla inversion model performance were evaluated by the coefficient of determination (R^2), the mean squared error (MSE), and the mean absolute error (MAE).

$$R^2 = 1 - \frac{\sum_{i=1}^{n}(\hat{y}_i - y_i)^2}{\sum_{i=1}^{n}(\bar{y}_i - y_i)^2} \quad (20)$$

$$MSE = \frac{1}{n}\sum_{i=1}^{n}(\hat{y}_i - y_i)^2 \quad (21)$$

$$MAE = \frac{1}{n}\sum_{i=1}^{n}|\hat{y}_i - y_i| \quad (22)$$

where y_i is the measured value, $\hat{y}_i$ is the predicated value, and n is the number of samples. The higher the R^2 value and the lower the MSE and MAE values, the higher the accuracy of the model.

4. Results

4.1. Inversion results for the IOPs obtained using field-measured spectra

4.1.1. $b_{bp}(\lambda)$

The inversion of $b_{bp}(\lambda)$ utilized an optimized method with dual-band, while single-band inversion was conducted using 550 nm and 677 nm, respectively. The mean values of the simulated $b_{bp}(\lambda)$ and the $b_{bp}(\lambda)$ inverted from the three different models are shown in Fig. 5. The simulated $b_{bp}(\lambda)$ exhibits certain fluctuations in the range of 500 to 600 nm, which cannot be characterized well by a single band. The overall R^2 values using $b_{bp}550$ and $b_{bp}677$ are 0.8962 and 0.9257, respectively; the MSE values are 0.019 and 0.014, respectively; and the MAE values are 0.096 and 0.081, respectively. By utilizing dual-band for the optimization, the variation characteristics can be characterized well, and its mean curve is highly consistent with the simulated $b_{bp}(\lambda)$. The overall R^2 value reaches 0.9649, and the MSE and MAE are reduced to 0.006 and 0.056, respectively, which is a significant improvement when compared to the traditional power function fitting method with a single band.

4.1.2. $a(\lambda)$

Fig. 6 Shows a comparison of the mean values between the measured $a(\lambda)$ and calculated $a(\lambda)$, where the shaded area is one standard deviation around the mean value. From the graph, it can be seen that the

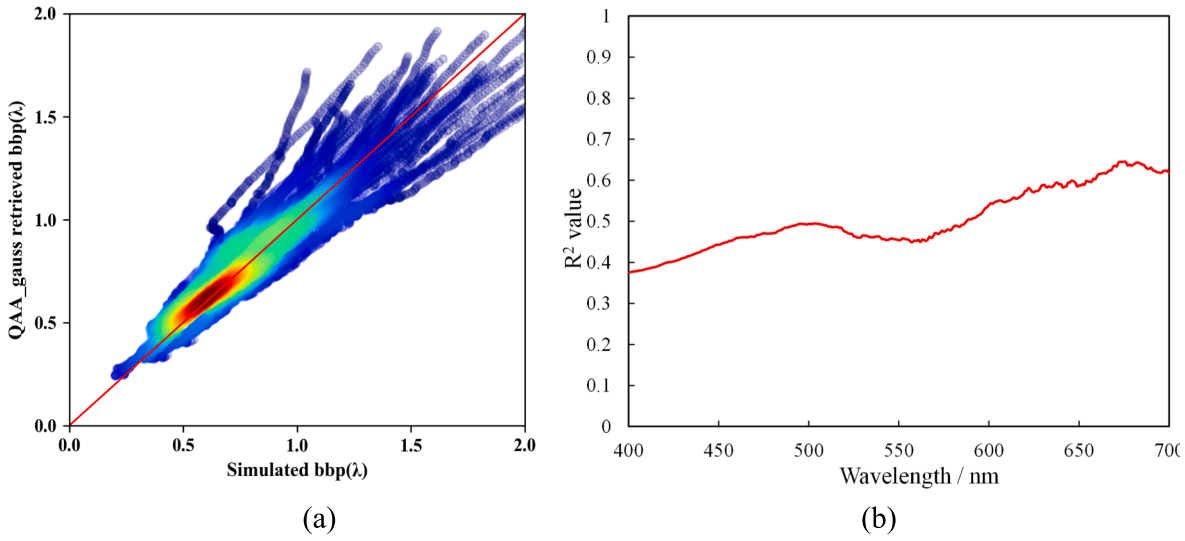

Fig. 13. Distribution and accuracy of the calculated $b_{bp}(\lambda)$ obtained using the airborne hyperspectral images. (a) Density scatter plot. (b) R^2 distribution for each band.

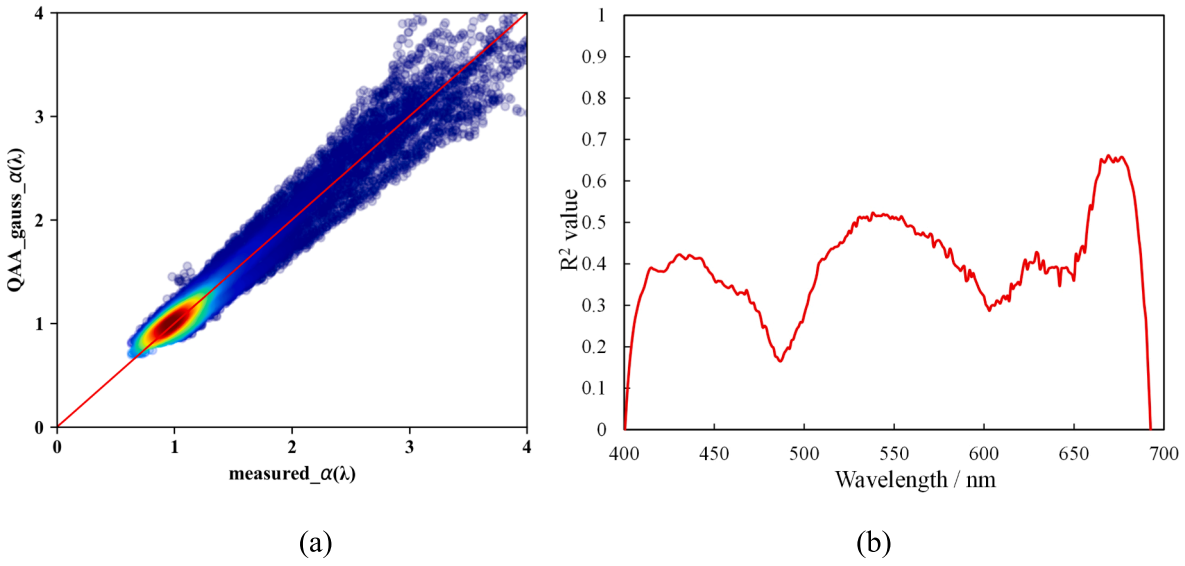

Fig. 14. Distribution and accuracy of the calculated $a(\lambda)$ obtained using the airborne hyperspectral images. (a) Density scatter plot. (b) R^2 distribution for each band.

calculated $a(\lambda)$ has a high consistency with the overall trend of the measured values. Fig. 7(a) shows the overall scatter distribution of the measured and calculated values, which is distributed near the 1:1 line. The overall R^2 is 0.9627 and the MSE and MAE are 0.0117 and 0.0886, respectively. Fig.7(b) shows the R^2 distribution of each band. The inversion accuracy is relatively high near 420 nm, 550 nm, and 670 nm, with R^2 values over 0.6 and some bands reaching 0.8. Here, six representative bands were selected for evaluation. The scatter plot distribution and accuracy evaluation are provided in Fig. 8 and Table 4, respectively.

4.1.3. $a_{ph}(\lambda)$

The first step in using $a(\lambda)$ decomposition to obtain $a_{ph}(\lambda)$ is to construct a Gaussian simulation function. The measured $a_{ph}677$ was utilized to obtain the parameters of the Gaussian simulation function. The simulation diagram based on the Gaussian function is shown in Fig. 9(a).The simulation accuracy R^2 of each band is shown in the red curve in Fig. 10. It can be seen that the simulation accuracy is high. Except for the lower R^2 value in the range of 500–600 nm, the R^2 value for all the other bands exceeds 0.9.

After that, the calculated $a(\lambda)$ and the regression relationship in Eq. (14) were utilized to simulate $a_{ph}(\lambda)$. The simulation accuracy is shown in the blue curve in Fig. 10, which is consistent with the distribution trend of the red curve. Except for the lower accuracy at 500 nm to 600 nm, the R^2 of all the other bands exceeds 0.6, and reaches above 0.8 near 675 nm. The R^2 value for the calculated a_{ph} is 0.8037.

In addition, we compared the algebraic decomposition methods proposed in the QAA_V6 algorithm to decompose $a(\lambda)$. The ratio relationship ξ, ζ of a_{dg} and a_{ph} at 412 nm and 443 nm, and the exponential decay slope S of a_{dg}, were obtained using empirical formulas through band optimization, finally obtaining $a_{ph}(\lambda)$. The simulation accuracy R^2 of each band is shown in the green curve in Fig. 9(b). It can be seen that the R^2 value of this method is negative before 500 nm, which means that the fitting accuracy is very poor. We selected 440 nm, 550 nm, and 670 nm for the evaluation of the two different decomposition methods. The evaluation results are listed in Table 5.

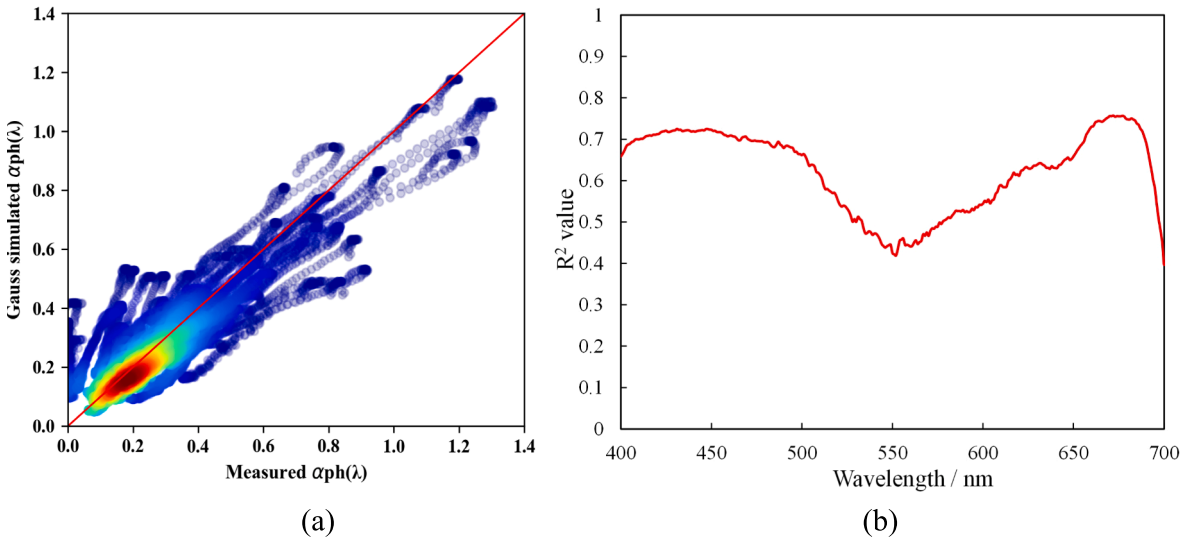

Fig. 15. Distribution and accuracy of the calculated $a_{ph}(\lambda)$ obtained using the airborne hyperspectral images. (a) Density scatter plot. (b) R^2 distribution for each band.

Table 7
Inversion accuracy for the IOPs at 440 nm, 550 nm, and 670 nm obtained using the airborne hyperspectral images.

Wavelength (nm)	IOPs	R^2	MSE	MAE
440 nm	$b_{bp}(\lambda)$	0.4258	0.0757	0.1986
	$a(\lambda)$	0.4128	0.0477	0.1840
	$a_{ph}(\lambda)$	0.7193	0.0296	0.1361
550 nm	$b_{bp}(\lambda)$	0.4538	0.0271	0.1240
	$a(\lambda)$	0.5093	0.0074	0.0706
	$a_{ph}(\lambda)$	0.4250	0.0054	0.0575
670 nm	$b_{bp}(\lambda)$	0.6349	0.0078	0.0667
	$a(\lambda)$	0.6565	0.0081	0.0771
	$a_{ph}(\lambda)$	0.7557	0.0093	0.0792
Overall	$b_{bp}(\lambda)$	0.7520	0.0386	0.1311
	$a(\lambda)$	0.9590	0.0212	0.1051
	$a_{ph}(\lambda)$	0.7727	0.0108	0.0768

4.2. Correction results for the airborne hyperspectral images

After image correction, we obtained the R_{rs} data for the study area. The overall mosaicked image of the water bodies is shown in Fig. 10. We evaluated the image R_{rs} using the measured R_{rs} data. The density scatter plot of the measured and calculated $R_{rs}(\lambda)$ is shown in Fig. 11(a). The overall R^2 value is 0.9498. The R^2 distribution of each band is shown in Fig. 11(b). In the range of 500 nm to 800 nm, the R^2 value is greater than 0.6, especially in the range of 600 nm to 700 nm, where the R^2 value is greater than 0.75. The highest accuracy is near 670 nm, with R^2 reaching a maximum of 0.8403. In addition, the IOP inversion bands were selected for evaluation. The scatter plot and accuracy evaluation are provided in Fig. 12 and Table 6, respectively. Except for the relatively low R^2 value at 425 nm, all the other bands exceed 0.65, and reach 0.8065 at 687 nm.

4.3. Inversion results for the IOPs obtained using the airborne hyperspectral images

After completing the image correction, the QAA_gauss model was applied to the airborne hyperspectral images, and the inversion results for $b_{bp}(\lambda)$, $a(\lambda)$, and $a_{ph}(\lambda)$ were obtained. The density scatter plots and the R^2 distribution for all bands are shown in Figs. 13-15. The overall inversion accuracy for the three IOPs is high, and the scatter points are uniformly distributed near the 1:1 line. However, in some green and blue bands, especially around 400–500 nm, the inversion accuracy of R^2 is relatively low, and the corresponding IOPs values are relatively large, resulting in a certain dispersion in high-value areas of the scatter plot.

The overall R^2 of $b_{bp}(\lambda)$ is 0.7520, and the distribution is in the range of 0.2 to 1.2. Due to the approximate exponential distribution, the variation is significant in the shorter wavelength, leading to the distribution divergence shown in Fig. 13(a). As shown in Fig. 13(b), the overall R^2 variation is relatively small, with the lowest accuracy in the shorter wavelength, and the highest accuracy near 670 nm, reaching over 0.6.

The inversion accuracy for $a(\lambda)$ is relatively high, with the overall R^2 reaching 0.9590, and it can be seen from the distribution of the scatter point density in Fig. 14(a) that the scatter points are uniformly distributed around the 1:1 line. The R^2 distribution shown in Fig. 14(b) is relatively consistent with the distribution for the ground model, and a high inversion accuracy has been achieved near 440 nm, 550 nm, and 670 nm. The R^2 at 670 nm reaches 0.65.

The overall R^2 of $a_{ph}(\lambda)$ is 0.7727, with a relatively concentrated distribution in the range of 0.2 to 0.4. From Fig. 15(b), it can be seen that the R^2 accuracy exceeds 0.6 in the band range of 400 nm to 510 nm, and 615 nm to 695 nm, with the highest accuracy reaching 0.7568 at 672 nm.

We selected 440 nm, 550 nm, and 670 nm for quantitative evaluation. The accuracy is listed in Table 7. The inversion maps are shown in Fig. 16.

4.4. Inversion results for Chla

The Chla inversion model was established based on the ground-measured $a_{ph}(677)$ and R_{rs}. After completing the inversion model, we utilized the $a_{ph}(677)$ obtained in Section 4.3 and the R_{rs} images as input parameters for the Chla inversion and mapping. The inversion results for a total of ten models with different input parameter combinations are shown in Table 8. When using $a_{ph}(677)$ and $R_{rs}(510)/[R_{rs}(556)\text{-}R_{rs}(673)]$ as bivariates for the binary linear model construction, the ground spectral inversion accuracy R^2 is 0.8139, and the hyperspectral imagery inversion result is the highest, reaching 0.7520. The Chla concentration spatial distribution result is shown in Fig. 17. The concentration of Chla in the river channels is significantly lower than that in the lakes and reservoirs. The Chla concentration in the study area is below 20 μg/L, with a Chla concentration of about 12 μg/L in Dianshan Lake and about 5 μg/L in the Taipu River.

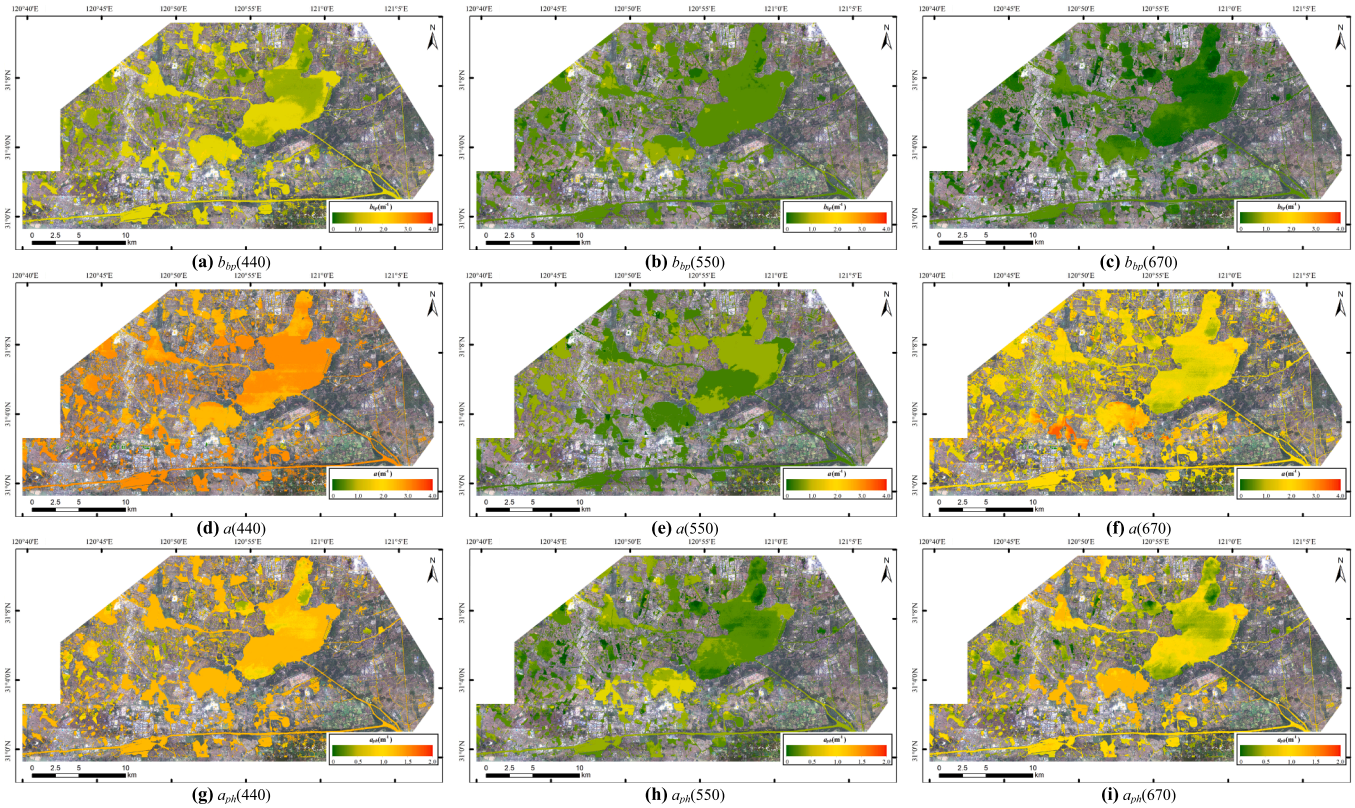

Fig. 16. The inversion maps of IOPs for the study area.

Table 8
Inversion results for Chla.

Input parameters	Inversion model	Ground spectra			Hyperspectral imagery		
		R^2	MSE	MAE	R^2	MSE	MAE
$a_{ph}(677)$	$29.548x - 3.031$	0.6978	7.7240	2.2207	0.6440	7.7240	2.1374
	$-35.833x^2 + 58.24x - 7.56$	0.6984	7.6054	2.2172	0.6750	6.8842	2.0172
	$28.663x^{-1.259}$	0.6710	8.2411	2.4089	0.6517	7.5563	2.1789
$R_{rs}(677)$	$-466.23x + 17.8998$	0.5121	12.2209	2.8492	0.5100	10.6310	2.5293
	$14975.98x^2 - 1226.35x + 26.65$	0.5678	10.8263	2.6560	0.4325	12.3128	2.6646
	$0.0374x^{-1.344}$	0.5147	12.1569	2.9708	0.2787	15.6512	3.1411
$\frac{R_{rs}(672)}{R_{rs}(563)}$	$-40.019x + 30.308$	0.7852	5.3810	1.6847	0.6765	7.0185	2.1140
	$19.852x^2 - 62.735x + 36.425$	0.7862	5.3549	1.6708	0.6671	7.2226	2.1192
	$1.168x^{-2.872}$	0.7323	6.7046	1.9774	0.5374	10.0375	2.4142
$\frac{R_{rs}(563)\text{-}R_{rs}(673)}{R_{rs}(563)+R_{rs}(673)}$	$48.916x - 6.3345$	0.7854	5.3754	1.6743	0.6640	7.2897	2.1189
	$-18.719x^2 + 59.536x - 7.676$	0.7858	5.3644	1.6728	0.6714	7.1292	2.1145
	$78.543x^{1.930}$	0.7728	5.6915	1.7555	0.6223	8.1949	2.1785
$\frac{R_{rs}(510)}{R_{rs}(556)\text{-}R_{rs}(673)}$	$-6.278x + 20.503$	0.7768	5.5906	1.7431	0.6939	6.6411	2.1761
	$2.865x^2 - 18.924x + 33.038$	0.8165	4.5959	1.5229	0.6964	6.5870	1.9991
	$21.982x^{1.894}$	0.7936	5.1686	1.7139	0.6160	8.3319	2.2331
$(\frac{1}{R_{rs}(562)}-\frac{1}{R_{rs}(671)})\times R_{rs}(664)$	$34.694x - 8.434$	0.7956	5.1195	1.6585	0.6765	7.0202	2.0949
	$10.916\ x^2 + 24.699{-}6.337$	0.7962	5.1050	1.6630	0.6685	7.1917	2.1009
	$39.804x^{2.289}$	0.7885	5.2966	1.7242	0.6318	7.9894	2.1687
$a_{ph}(677)$, $\frac{R_{rs}(672)}{R_{rs}(563)}$	$11.267x - 28.20y + 19.617$	0.8159	4.6113	1.5674	0.7257	5.9518	1.8215
	$-9.480x^2 + 19.572x - 18.834y^2 - 5.355y + 11.427$	0.8197	4.5170	1.5688	0.7423	5.5922	1.8386
	$0.677x^{-3.024} + 11.822y^{1.439}$	0.7565	6.0996	1.9358	0.6103	8.4552	2.1569
$a_{ph}(677)$, $\frac{R_{rs}(563)\text{-}R_{rs}(673)}{R_{rs}(563)+R_{rs}(673)}$	$10.895x + 34.532x - 6.136$	0.8127	4.6923	1.5839	0.7129	6.2303	1.8456
	$-8.209x^2 + 18.923x\text{-}63.264y^2 + 68.275y - 11.67$	0.8208	4.4897	1.5614	0.7469	5.4908	1.8282
	$9.202x^{1.449} + 61.805y^{2.02}$	0.7889	5.2876	1.7231	0.6639	7.2923	1.9810
$a_{ph}(677)$, $(\frac{1}{R_{rs}(562)}-\frac{1}{R_{rs}(671)})\times Rrs(664)$	$9.739x + 25.568y - 7.637$	0.8164	4.5990	1.5693	0.7195	6.0865	1.8548
	$-11.833x^2 + 20.01x\text{-}13.737y^2 + 36.915y - 11.582$	0.8218	4.4644	1.5564	0.7380	5.6855	1.8679
	$6.139x^{1.314} + 33.628y^{2.392}$	0.7957	5.1179	1.6935	0.6609	7.3566	2.0308
$a_{ph}(677)$, $\frac{R_{rs}(510)}{R_{rs}(556)\text{-}R_{rs}(673)}$	**$12.025x - 4.282y + 12.185$**	**0.8139**	**4.6621**	**1.5956**	**0.7520**	**5.3810**	**1.8284**
	$-10.687x^2 + 15.52x + 2.199y^2 - 14.711y + 23.617$	0.8283	4.2995	1.4968	0.7308	5.8403	1.8790
	$3.692x^{1.347} + 19.609y^{-1.93}$	0.7957	5.1167	1.7037	0.6340	7.9421	2.1627

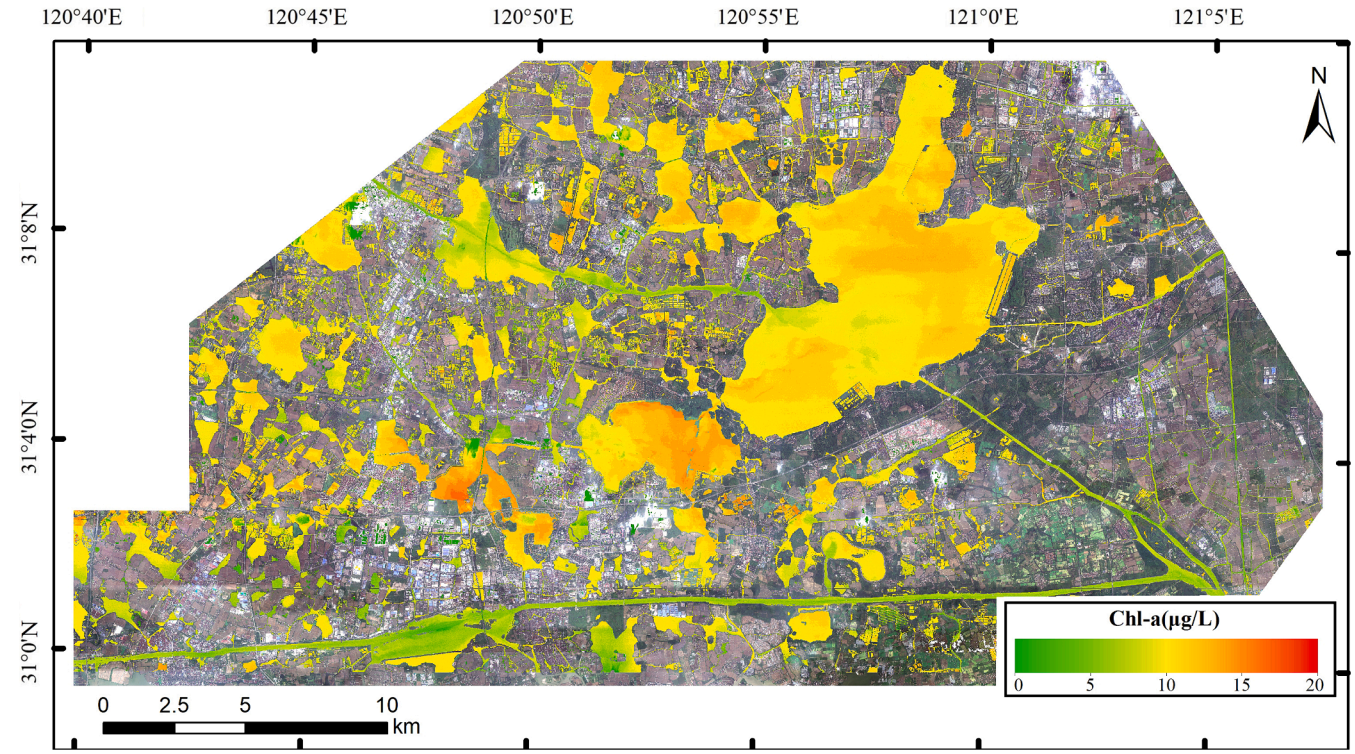

Fig. 17. The Chla concentration spatial distribution for the study area.

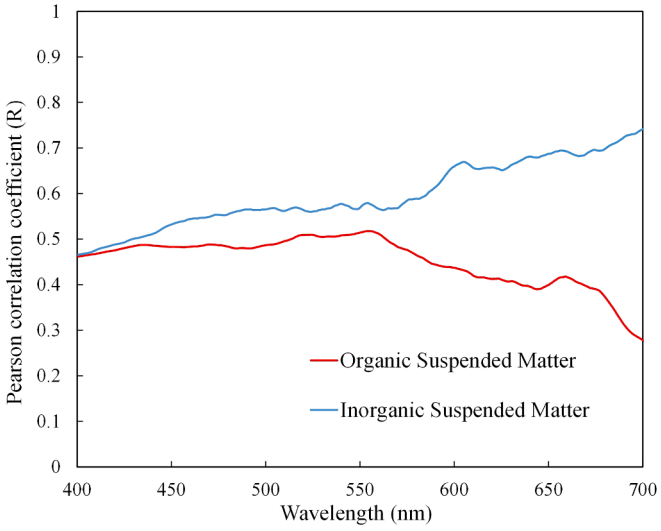

Fig. 18. The correlation between the backscatter coefficient and organic and inorganic suspended matter.

5. Discussion

5.1. Analysis of the model accuracy

The QAA_gauss model proposed in this paper focuses on the water color characteristics of the study area, optimizes the reference wavelengths and semi-empirical parameters using measured data, and constructs a regional optimized IOP inversion algorithm. The model can effectively invert the IOPs, including $b_{bp}(\lambda)$, $a(\lambda)$, and $a_{ph}(\lambda)$. From the IOPs and Chla concentration distribution obtained from the airborne hyperspectral images, it can be seen that the proposed model can achieve good results for the lakes, reservoirs, and rivers with varying optical characteristics in the study area.

Due to the complex optical characteristics of inland water bodies, the visible bands lose sensitivity to $b_{bp}(\lambda)$, resulting in significant errors in $b_{bp}(\lambda)$ inversion (Shi et al., 2019). In addition, a large number of measured results also indicate that the backscattering characteristics of inland water bodies may not exhibit exponential characteristics (Lin et al., 2018). The use of a dual-band joint inversion strategy can effectively alleviate the low accuracy using a single band. At the same time, the dual-band approach can better characterize the distribution characteristics of $b_{bp}(\lambda)$ in regional water bodies.

We compared the correlation between b_{bp} and organic–inorganic particulate matter, and found distinct differences in the correlations among various types of particulate matter shown in Fig. 18. For OSM, its correlation with $b_{bp}(\lambda)$ increases in the range 400–550 nm, reaches its peak near 550 nm. After 550 nm, the correlation gradually decreases. Different from OSM, ISM shows a consistent upward trend with increasing wavelength, which indicates that the use of dual-band has potential for estimating concentration of different particle types and revealing the influence of particles on $b_{bp}(\lambda)$. Since the backscattering coefficient is influenced by the interaction of inorganic and organic particulate matter, and the strong absorption characteristics of organic particles can affect b_{bp} (Shi et al., 2014), the inversion accuracy of the $b_{bp}(\lambda)$ is relatively low in the blue and green spectra before 550 nm, which are highly correlated with organic particles. This also leads to a significantly lower R^2 of $a(\lambda)$ in this region compared to the region after 550 nm.

In the QAA algorithm, empirical ratio estimation is utilized to decompose $a(\lambda)$, and the ratio parameters ξ, ζ of a_{dg} and a_{ph} need to be calculated separately. In addition, empirical formulas are also required to obtain the exponential decay slope S of a_{dg}. Although we optimized the empirical parameters using the measured IOPs, the results show that the calculated $a_{ph}(\lambda)$ does not fit well before 500 nm. In addition to the accumulation of errors caused by the large number of steps required for the empirical ratio solution, the use of a single empirical shape or single slope as an empirical model of a_{dg} can cause significant errors within a shorter wavelength range (Werdell et al., 2013; Zhang et al., 2015). The

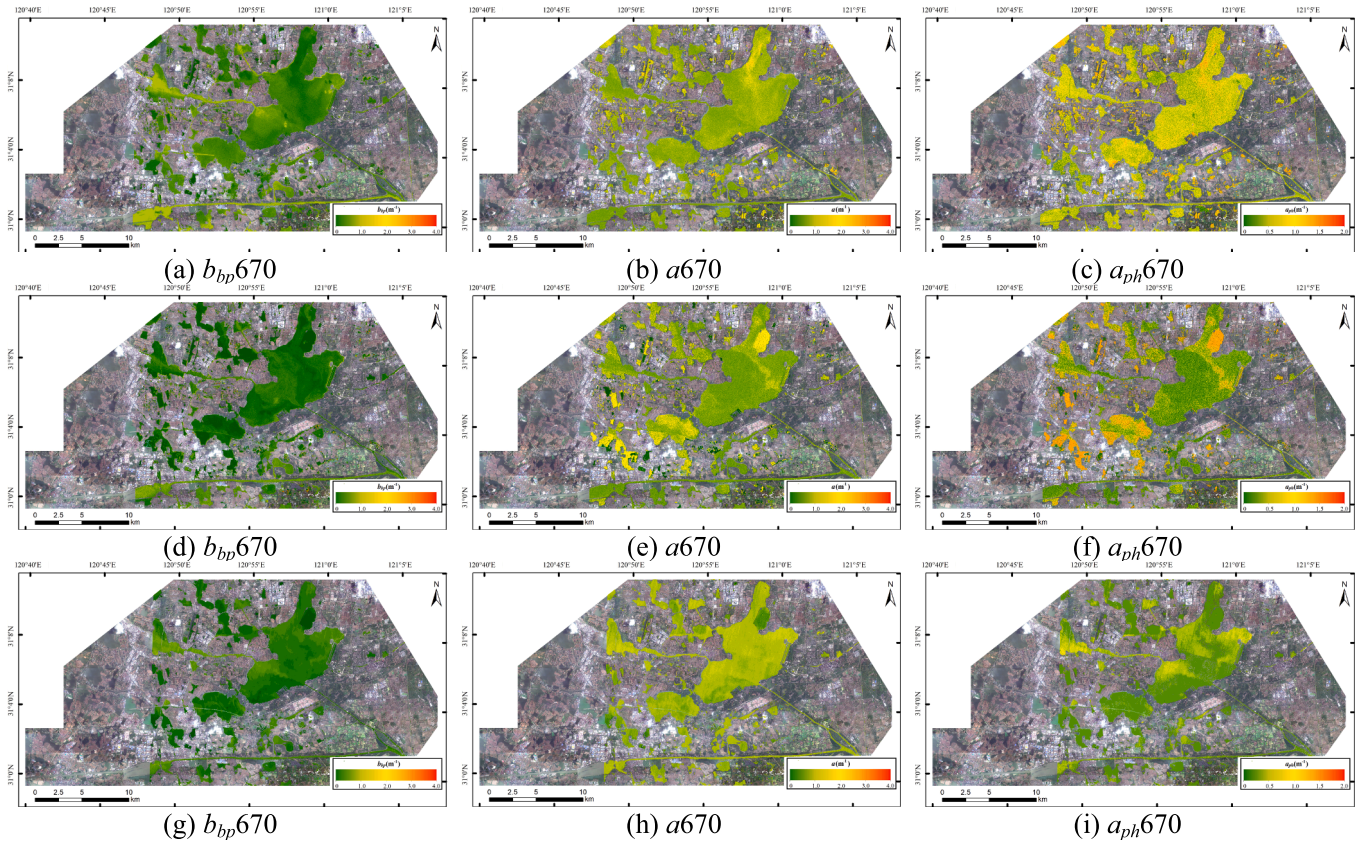

Fig. 19. The inversion maps of IOPs at 670 nm for the study area using satellite hyperspectral imagery. (a)–(c) November 18, 2021. (d)–(f) December 25, 2022. (g)–(i) March 6, 2023.

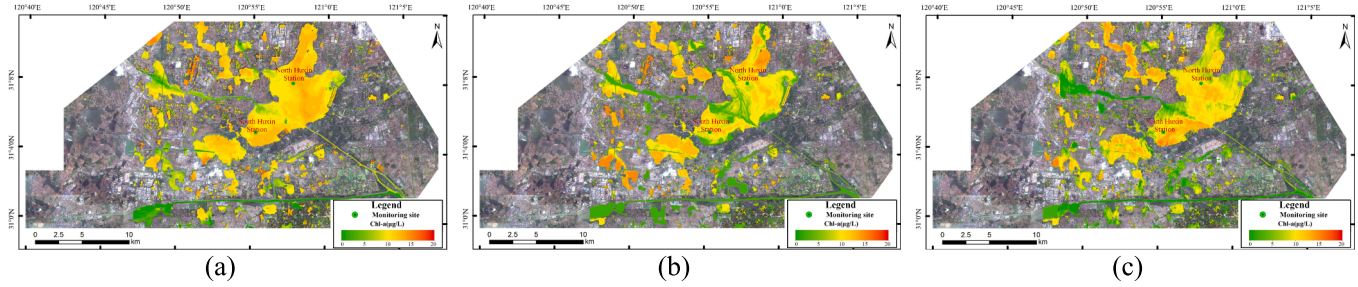

Fig. 20. The Chla concentration spatial distribution for the study area using satellite hyperspectral imagery. (a) November 18, 2021. (b) December 25, 2022. (c) March 6, 2023.

Table 9
Inversion accuracy for Chla using satellite hyperspectral imagery.

Image acquisition date	Station name	Measured value (ug/L)	Inversion value (ug/L)	Mean absolute error (%)
2021/11/18	North Huxin	9.27	11.09	19.8274
	South Huxin	14.70	12.13	17.4714
2022/12/25	North Huxin	14.69	12.59	14.2743
	South Huxin	9.83	9.22	6.1953
2023/03/06	North Huxin	13.06	10.52	19.4410
	South Huxin	9.50	8.62	9.2736

proposed $a_{ph}(\lambda)$ decomposition method based on a Gaussian function utilizes $a_{ph}(677)$ to simulate the full spectral range of $a_{ph}(\lambda)$. By directly constructing a linear relationship between $a(\lambda)$ and $a_{ph}(677)$, the overall inversion accuracy is effectively improved. This indicates that the method based on a Gaussian function can effectively represent the absorption characteristics of $a_{ph}(\lambda)$. Since the prediction accuracy is not affected by a_{dg}, this can ensure the stability of the overall prediction accuracy of $a_{ph}(\lambda)$.

In the inversion modeling of Chla, it can be found that, when using a single variable for the modeling, $a_{ph}(677)$ has a relatively high correlation with Chla, and the inversion accuracy R^2 is greater than 0.6. Using only a single R_{rs} band for modeling is not effective, the single band be affected by incomplete atmospheric correction, resulting in significant errors (Ruddick et al., 2001). After performing the dual-band or three-band mathematical operations, the inversion accuracy is significantly improved. However, the characteristics of R_{rs} may not directly reflect changes of Chla, which may lead to misjudgment using purely empirical

models (Lee et al., 2020). Compared to the univariate inversion model, the R^2 value of the bivariate inversion model using both $a_{ph}(677)$ and R_{rs} is increased by about 10 %. A possible reason for this is that the dependency relationship (ratio relationship) between a_{ph} and Chla can affect the accuracy of algorithms using R_{rs}, especially in a relatively small range of Chla of about 5 to 10 mg/m^3 (Gilerson et al., 2010). In addition, the proportion of detritus particles in a small Chla concentrations and the pigment packaging effect also limited the accuracy of using a single a_{ph} for inversion. The inversion model that considers both a_{ph} and R_{rs} can compensate for the shortcomings of the univariate inversion and improve the inversion accuracy.

However, due to the significant differences in the optical properties of different inland water bodies, the empirical formula parameters proposed in this paper may not be applicable to other water bodies. In future research, introducing optical classification of water optical characteristics should be considered and different regions should be modeled separately (Jiang et al., 2020).

5.2. Application using satellite hyperspectral imagery

Due to the high cost of obtaining airborne hyperspectral images, we only obtained single-temporal image data in this study, so that we could not conduct a temporal analysis. In recent years, spaceborne hyperspectral sensors have developed rapidly, and hyperspectral satellites with a high spatial resolution and width, have achieved success in monitoring inland water bodies(Liu et al., 2022).

To further validate the applicability of the model, we utilized ZY1-02D and ZY1-02E Advanced Hyperspectral Imager (AHSI) for long-term monitoring. The AHSI VNIR sensor covers a spectral range of 400–1000 nm, with a total of 76 bands. We selected cloud-free images covering our main research area, which were obtained on November 18, 2021, December 25, 2022, and March 6, 2023, respectively. We applied the proposed model to invert IOPs and Chla. The inversion maps of IOPs at 670 nm and Chla are shown in Fig.19 and Fig. 20, respectively.

To quantitatively evaluate the inversion accuracy, we assess the inversion quantitative accuracy by the Chla monitoring data on two monitoring stations (North Huxin and South Huxin) in the Dianshan Lake at the satellite imaging time from the Shanghai Environmental Monitoring Center, as shown in Fig. 1. The comparison results between the measured values and the inversion values are reported in Table 9. The mean absolute errors are all less than 20 %, with an average error of about 14.4 %, proving the applicability of the model to hyperspectral satellite imagery.

Due to the lack of sampling data at the satellite imaging time, we were unable to evaluate the inversion accuracy of IOPs. In addition, limited by the meteorological conditions in the study area and revisit interval of hyperspectral satellite, only a small portion of hyperspectral data can be used for inversion applications. This poses challenges for long-term monitoring, however, with the ongoing development of hyperspectral satellites, the sources of hyperspectral data are becoming more abundant and accessible. In the future, a long-term application analysis could be considered using satellite hyperspectral image data.

6. Conclusion

In this paper, a semi-analytical approach for estimating inland water IOPs has been proposed, which was applied to key lakes, reservoirs, and rivers in the Yangtze River Delta Integrated Demonstration Zone. The model is based on the QAA algorithm, and the measured IOPs and R_{rs} are employed for optimizing the regional empirical parameters. At the same time, the solving process of b_{bp} and a_{ph} is optimized using a dual-band joint inversion strategy and a Gaussian function fitting method, which can obtain high-precision IOPs. At the same time, an inversion model is constructed for Chla, which takes into account both a_{ph} and R_{rs}. The proposed method has a better accuracy than the univariate inversion model.

In order to apply the ground model to airborne hyperspectral images, a high-precision water reflectance inversion process was constructed. Based on the radiative transfer model for water bodies, combined with the measured atmospheric parameters and measured reflectance spectra, the water-leaving reflectance of the airborne hyperspectral images was obtained, ensuring the effect of the ground model. Finally, the spatial mapping of the IOPs and Chla was completed, which will be of great significance for subsequent water quality analyses. The experiment demonstrated that the proposed semi-analytical method exhibits good performance, and has been successfully applied to long-term monitoring using satellite hyperspectral images, highlighting the significant potential of hyperspectral remote sensing for high-precision monitoring of regional water bodies.

CRediT authorship contribution statement

Chao Niu: Writing – original draft, Validation, Methodology, Investigation, Data curation. **Kun Tan:** Writing – review & editing, Validation, Resources, Project administration, Funding acquisition, Data curation. **Xue Wang:** Writing – review & editing, Supervision. **Peijun Du:** Writing – review & editing. **Chen Pan:** Data curation, Conceptualization.

Declaration of competing interest

The authors declare that they have no known competing financial interests or personal relationships that could have appeared to influence the work reported in this paper.

Data availability

No data was used for the research described in the article.

Acknowledgements

This research is jointly supported by the Shanghai Municipal Science and Technology Major Project (No. 22511102800), National Natural Science Foundation of China (No. 42171335), National Civil Aerospace Project of China (No. D040102) and the International Research Center of Big Data for Sustainable Development Goals(No. CBAS2022GSP07).

References

Allison, D.B., Stramski, D., Mitchell, B.G., 2010. Empirical Ocean color algorithms for estimating particulate organic carbon in the Southern Ocean. J. Geophys. Res.: Oceans 115.
Berk, A., Bernstein, L.S., Robertson, D.C., 1989. MODTRAN: a moderate resolution model for LOWTRAN 7. Geophysics Laboratory Hanscom AFB, MA, USA.
Bricaud, A., Babin, M., Morel, A., Claustre, H., 1995. Variability in the chlorophyll-specific absorption coefficients of natural phytoplankton: analysis and parameterization. J. Geophys. Res. Oceans 100, 13321–13332.
Chase, A., Boss, E., Zaneveld, R., Bricaud, A., Claustre, H., Ras, J., Dall'Olmo, G., Westberry, T.K., 2013. Decomposition of in situ particulate absorption spectra. Methods Oceanography 7, 110–124.
Cleveland, J.S., 1995. Regional models for phytoplankton absorption as a function of chlorophyll a concentration. J. Geophys. Res. Oceans 100, 13333–13344.
Doxaran, D., Babin, M., Leymarie, E., 2007. Near-infrared light scattering by particles in coastal waters. Opt. Express 15, 12834–12849.
Doxaran, D., Ruddick, K., McKee, D., Gentili, B., Tailliez, D., Chami, M., Babin, M., 2009. Spectral variations of light scattering by marine particles in coastal waters, from the visible to the near infrared. Limnol. Oceanogr. 54, 1257–1271.
Gilerson, A.A., Gitelson, A.A., Zhou, J., Gurlin, D., Moses, W., Ioannou, I., Ahmed, S.A., 2010. Algorithms for remote estimation of chlorophyll-a in coastal and inland waters using red and near infrared bands. Opt. Express 18, 24109–24125.
Gordon, H.R., Brown, O.B., Evans, R.H., Brown, J.W., Smith, R.C., Baker, K.S., Clark, D. K., 1988. A semianalytic radiance model of ocean color. J. Geophys. Res. Atmos. 93, 10909–10924.
Gordon, H.R., Morel, A.Y., 1983. Remote assessment of ocean color for interpretation of satellite visible imagery: a review. Springer-Verlag.
He, J., Chen, Y., Wu, J., Stow, D.A., Christakos, G., 2020. Space-time chlorophyll-a retrieval in optically complex waters that accounts for remote sensing and modeling uncertainties and improves remote estimation accuracy. Water Res. 171, 115403.

Hoepffner, N., Sathyendranath, S., 1991. Effect of pigment composition on absorption properties of phytoplankton. Mar. Ecol. Prog. Ser 73, 11–23.
Hoepffner, N., Sathyendranath, S., 1993. Determination of the major groups of phytoplankton pigments from the absorption spectra of total particulate matter. J. Geophys. Res. Oceans 98, 22789–22803.
Hoge, F.E., Lyon, P.E., 1996. Satellite retrieval of inherent optical properties by linear matrix inversion of oceanic radiance models: an analysis of model and radiance measurement errors. J. Geophys. Res. Oceans 101, 16631–16648.
Hu, C., Lee, Z., Franz, B., 2012. Chlorophyll aalgorithms for oligotrophic oceans: a novel approach based on three-band reflectance difference. J. Geophys. Res. Oceans 117.
Jia, J., Chen, J., Zheng, X., Wang, Y., Guo, S., Sun, H., Jiang, C., Karjalainen, M., Karila, K., Duan, Z., 2021. Tradeoffs in the spatial and spectral resolution of airborne hyperspectral imaging systems: a crop identification case study. IEEE Trans. Geosci. Remote Sens. 60, 1–18.
Jiang, G., Loiselle, S.A., Yang, D., Ma, R., Su, W., Gao, C., 2020. Remote estimation of chlorophyll a concentrations over a wide range of optical conditions based on water classification from VIIRS observations. Remote Sens. Environ. 241, 111735.
Kim, J., Jang, W., Kim, J.H., Lee, J., Cho, K.H., Lee, Y.-G., Chon, K., Park, S., Pyo, J., Park, Y., 2022. Application of airborne hyperspectral imagery to retrieve spatiotemporal CDOM distribution using machine learning in a reservoir. Int. J. Appl. Earth Obs. Geoinf. 114, 103053.
Lee, Z., Carder, K.L., Steward, R., Peacock, T., Davis, C., Patch, J., 1998. An empirical algorithm for light absorption by ocean water based on color. J. Geophys. Res. Oceans 103, 27967–27978.
Lee, Z., Carder, K.L., Arnone, R.A., 2002. Deriving inherent optical properties from water color: a multiband quasi-analytical algorithm for optically deep waters. Appl. Opt. 41, 5755–5772.
Lee, Z., Lubac, B., Werdell, J., Arnone, R., 2014. Update of the quasi-analytical algorithm (QAA_v6). International Ocean Color Group Software Report. http://www.ioccg.org/groups/Software_OCA/QAA_v6_2014209.pdf.
Lee, Z., Shang, S., Zhang, S., Wu, J., Wei, G., Wu, X., 2020. Impact of temporal variation of chlorophyll-specific absorption on phytoplankton phenology observed from ocean color satellite: a numerical experiment. J. Geophys. Res. Oceans 125, e2020JC016382.
Lin, J., Lee, Z., Ondrusek, M., Liu, X., 2018. Hyperspectral absorption and backscattering coefficients of bulk water retrieved from a combination of remote-sensing reflectance and attenuation coefficient. Opt. Express 26, A157–A177.
Liu, G., Li, L., Song, K., Li, Y., Lyu, H., Wen, Z., Fang, C., Bi, S., Sun, X., Wang, Z., 2020. An OLCI-based algorithm for semi-empirically partitioning absorption coefficient and estimating chlorophyll a concentration in various turbid case-2 waters. Remote Sens. Environ. 239, 111648.
Liu, Y., Li, J., Xiao, C., Zhang, F., Wang, S., Yin, Z., Wang, C., Zhang, B., 2022. A classification-based, semianalytical approach for estimating water clarity from a hyperspectral sensor onboard the ZY1-02D satellite. IEEE Trans. Geosci. Remote Sens. 60, 1–14.
Lohrenz, S.E., Weidemann, A.D., Tuel, M., 2003. Phytoplankton spectral absorption as influenced by community size structure and pigment composition. J. Plankton Res. 25, 35–61.
Mitchell, B.G., 1990. Algorithms for determining the absorption coefficient for aquatic particulates using the quantitative filter technique. In: Ocean Optics x. SPIE, pp. 137–148.
Mobley, C.D., 1999. Estimation of the remote-sensing reflectance from above-surface measurements. Appl. Opt. 38, 7442–7455.
Mueller, J.L., Morel, A., Frouin, R., Davis, C., Arnone, R., Carder, K., Lee, Z., Steward, R., Hooker, S., Mobley, C., 2003. Ocean Optics Protocols For Satellite Ocean Color Sensor Validation, Revision 4. Volume III: Radiometric Measurements and Data Analysis Protocols. National Aeronautics and Space Administration, Goddard Space Flight Center.
Neil, C., Spyrakos, E., Hunter, P.D., Tyler, A.N., 2019. A global approach for chlorophyll-a retrieval across optically complex inland waters based on optical water types. Remote Sens. Environ. 229, 159–178.
Niu, C., Tan, K., Jia, X., Wang, X., 2021a. Deep learning based regression for optically inactive inland water quality parameter estimation using airborne hyperspectral imagery. Environ. Pollut. 286, 117534.
Niu, C., Tan, K., Wang, X., Han, B., Ge, S., Du, P., Wang, F., 2021b. Radiometric cross-calibration of the ZY1-02D hyperspectral imager using the GF-5 AHSI imager. IEEE Trans. Geosci. Remote Sens. 60, 1–12.
Ogashawara, I., Mishra, D.R., Nascimento, R.F., Alcântara, E.H., Kampel, M., Stech, J.L., 2016. Re-parameterization of a quasi-analytical algorithm for colored dissolved organic matter dominant inland waters. Int. J. Appl. Earth Obs. Geoinf. 53, 128–145.
Pan, H., Lyu, H., Wang, Y., Jin, Q., Wang, Q., Li, Y., Fu, Q., 2015. An improved approach to retrieve IOPs based on a quasi-analytical algorithm (QAA) for turbid eutrophic inland water. IEEE J. Sel. Top. Appl. Earth Obs. Remote Sens. 8, 5177–5189.
Ruddick, K.G., Gons, H.J., Rijkeboer, M., Tilstone, G., 2001. Optical remote sensing of chlorophyll a in case 2 waters by use of an adaptive two-band algorithm with optimal error properties. Appl. Opt. 40, 3575–3585.
Shi, K., Li, Y., Zhang, Y., Li, L., Lv, H., Song, K., 2014. Optical scattering properties of organic-rich and inorganic-rich particles in inland waters. J. Great Lakes Res. 40, 308–316.
Shi, W., Wang, M., Zhang, Y., 2019. Inherent optical properties in lake taihu derived from VIIRS satellite observations. Remote Sens. (Basel) 11, 1426.
Snyder, W.A., Arnone, R.A., Davis, C.O., Goode, W., Gould, R.W., Ladner, S., Lamela, G., Rhea, W.J., Stavn, R., Sydor, M., 2008. Optical scattering and backscattering by organic and inorganic particulates in US coastal waters. Appl. Opt. 47, 666–677.
Stuart, V., Sathyendranath, S., Platt, T., Maass, H., Irwin, B.D., 1998. Pigments and species composition of natural phytoplankton populations: effect on the absorption spectra. J. Plankton Res. 20, 187–217.
Tan, K., Niu, C., Jia, X., Ou, D., Chen, Y., Lei, S., 2020. Complete and accurate data correction for seamless mosaicking of airborne hyperspectral images: a case study at a mining site in Inner Mongolia, China. ISPRS J. Photogramm. Remote Sens. 165, 1–15.
Tzortziou, M., Herman, J.R., Gallegos, C.L., Neale, P.J., Subramaniam, A., Harding Jr, L. W., Ahmad, Z., 2006. Bio-optics of the Chesapeake Bay from measurements and radiative transfer closure. Estuar. Coast. Shelf Sci. 68, 348–362.
Wanner, W., Li, X., Strahler, A., 1995. On the derivation of kernels for kernel-driven models of bidirectional reflectance. J. Geophys. Res. Atmos. 100, 21077–21089.
Wen, Z., Wang, Q., Liu, G., Jacinthe, P.-A., Wang, X., Lyu, L., Tao, H., Ma, Y., Duan, H., Shang, Y., 2022. Remote sensing of total suspended matter concentration in lakes across China using landsat images and Google earth engine. ISPRS J. Photogramm. Remote Sens. 187, 61–78.
Werdell, P.J., Franz, B.A., Bailey, S.W., Feldman, G.C., Boss, E., Brando, V.E., Dowell, M., Hirata, T., Lavender, S.J., Lee, Z., 2013. Generalized Ocean color inversion model for retrieving marine inherent optical properties. Appl. Opt. 52, 2019–2037.
Werdell, P.J., McKinna, L.I., Boss, E., Ackleson, S.G., Craig, S.E., Gregg, W.W., Lee, Z., Maritorena, S., Roesler, C.S., Rousseaux, C.S., 2018. An overview of approaches and challenges for retrieving marine inherent optical properties from ocean color remote sensing. Prog. Oceanogr. 160, 186–212.
Xu, J., Lei, S., Bi, S., Li, Y., Lyu, H., Xu, J., Xu, X., Mu, M., Miao, S., Zeng, S., 2020. Tracking spatio-temporal dynamics of POC sources in eutrophic lakes by remote sensing. Water Res. 168, 115162.
Xu, J., Bian, Y., Lyu, H., Miao, S., Li, Y., Liu, H., Xu, J., 2021. Estimation of particulate backscattering coefficient in turbid inland water using sentinel 3A-OLCI image. IEEE J. Sel. Top. Appl. Earth Obs. Remote Sens. 14, 8577–8593.
Zhan, H., Lee, Z., Shi, P., Chen, C., Carder, K.L., 2003. Retrieval of water optical properties for optically deep waters using genetic algorithms. IEEE Trans. Geosci. Remote Sens. 41, 1123–1128.
Zhang, X., Huot, Y., Bricaud, A., Sosik, H.M., 2015. Inversion of spectral absorption coefficients to infer phytoplankton size classes, chlorophyll concentration, and detrital matter. Appl. Opt. 54, 5805–5816.
Zhu, W., Yu, Q., 2012. Inversion of chromophoric dissolved organic matter from EO-1 hyperion imagery for turbid estuarine and coastal waters. IEEE Trans. Geosci. Remote Sens. 51, 3286–3298.